Long range numerical simulation of acoustical shock waves in a 3D moving heterogeneous and absorbing medium

David Luquet, Régis Marchiano, François Coulouvrat

HAL Id: hal-04229059

https://hal.sorbonne-universite.fr/hal-04229059

Submitted on 5 Oct 2023

Long Range Numerical Simulation of Acoustical Shock Waves in a 3D Moving Heterogeneous and Absorbing Medium

David Luquet[a], Régis Marchiano[a,*], François Coulouvrat[a]

[a]*Sorbonne Universités, UPMC Univ Paris 06, CNRS, UMR 7190, Institut Jean Le Rond d'Alembert, F-75005 Paris, France*

Abstract

Acoustical shock waves can be generated by numerous atmospheric sources, either natural – like thunder and volcanoes – or anthropic – like explosions, sonic boom or buzz saw noise. The prediction of their long-range propagation remains a numerical challenge at 3D because of the large propagation distance to wavelength ratio, and of the high frequency / small wavelength content associated to shocks. In this paper, an original numerical method for propagating acoustical shock waves in three-dimensional heterogeneous media is proposed. Heterogeneities can result from temperature or density gradients and also from atmospheric shear and turbulent flows. The method called FLHOWARD (for FLow and Heterogeneities in a One-Way Approximation of the nonlineaR wave equation in 3D) is based on a one-way solution of a generalized nonlinear wave equation. Even though backscattering is neglected, it does not suffer from the limitations of classical ray theory nor from the angular limitations of the popular parabolic methods.

The numerical approach is based on a split-step method, which has the advantage of splitting the original equation into simpler ones associated with specific physical mechanisms: diffraction, flows, heterogeneities, nonlinearities, absorption and relaxation. The method has been developed on parallel architecture for very high demanding 3D configurations using the Single Method Multiple Data paradigm. The method is validated through several test cases. A study of the lateral cut-off of the sonic boom finally illustrates the potentialities of the method for realistic cases.

---

1. Introduction

Flow motion and medium inhomogeneities play a major role on the propagation of weak shock waves. Influence of atmospheric effects on acoustical shocks were already studied as early as the beginning of the twentieth century for loud sources such as accidental explosions, artillery bombings and volcanoes (see [1, 2] for reviews). For sonic boom [3], the wind stratification influences the pressure distribution on the ground [4, 5] while the turbulence in the planetary boundary layer alters the boom signatures [6, 7]. Buzz saw noise produced by turboengine fan blades running at top speed during take off propagates through flow in the inlet [8, 9]. Also nonlinear propagation through inhomogeneous atmosphere has been shown to be of major importance for jet noise [10], thunder [11], meteroids [12] or explosions [13]. The numerical simulation of such problems is a challenging issue requiring to combine: (1) low dispersion and dissipation schemes to cover propagation ranges reaching several hundreds of wavelengths, and (2) efficient shock capturing algorithms to capture the high frequency content of the spectrum.

2

The most common numerical approach is the nonlinear ray tracing method initially developed for sonic boom applications [14, 15]. It relies on the linear geometrical acoustic for determining the ray path, and then solve a nonlinear 1D transport equation along each ray to compute the waveform. However, this method relies on a high frequency approximation and does not take into account diffraction. Thus it cannot be employed for shadow zones in which it predicts no signal [16], caustics where the predicted amplitude is infinite [17, 18, 19] and scattering by turbulence.

Time-domain implementation of the Navier-Stokes equations (DNS) have the advantage to capture the full physics of the problem at the cost of a huge computational requirement. Low dispersion and dissipation explicit schemes adapted for aeroacoustics [20, 21] scales at 3D as power 4 of frequency and therefore are extremely demanding for capturing shocks. Some examples of applications [22, 23, 24] are either limited to 2D simulations, or require specific mesh refinement processes to follow the shock wave [25].

As a trade-off between the numerical efficiency of ray tracing and the precision of DNS lie one way methods. There is a huge litterature on one-way methods, ranging from parabolized Navier-Stokes equations to wide-angle parabolic wave equation. See for instance recent paper by Towne *et al.* [26] for linear hyperbolic systems and subsequent references. For linear acoustics, the standard [27] and wide-angle [28] parabolic approximations have been extensively used. In nonlinear acoustics, the nonlinear parabolic approximation known as the KZK equation [29, 30], is a one-way high frequency approach that takes into account nonlinearities and diffraction at the first order and therefore is valid only for small angles of propagation (typically $\pm 15^o$). It turned out highly successful in simulating high intensity collimated beams for ultrasonic biomedical applications [31, 32] or underwater

3

acoustics [33]. This method has been extended for long range atmospheric applications including the effect of slow flows [34] and applied at 2D to scattering of shock wave by turbulence [35]. Meanwhile, investigations have been carried out to overcome the angular limitation [36, 37, 38], and to extend them to 3D [39] but only for steady media. To our knowledge, the only model taking into account slow flow motion without angular limitation is the so called FLHOWARD model developed recently at 2D for a stratified flow [40].

The main objective of this work is to develop an efficient numerical method able to fully simulate weak shock waves propagation in a realistic three dimensional turbulent atmosphere. The present paper is an extension of the previous FLHOWARD model [40] to a 3D moving and heterogeneous medium. Also, absorption and dispersion mechanisms associated to thermo-viscosity and molecular relaxation are incorporated. The resulting implementation has been named FLHOWARD3D and has no angular limitation. Nevertheless it still relies on a one-way approach and therefore neglects the backscattered field. It is implemented on distributed memory architecture to allow for large computation and is extensively validated.

The main novelties of this study compared with the previous 2D version [40] are (i) the 3D parallel implementation for the propagation of acoustic shock waves through 3D velocity fields, (ii) the numerical analysis of the algorithm, (iii) the derivation of a numerical dispersion relation for wave propagation in a moving fluid (with a simplified formulation even more precise), (iv) the 3D validation tests, and finally (v) the application of the method to simulate the problem of sonic boom at the lateral cutoff.

The paper is organized as follows. In section 2, the physical basis of the model equation is recalled. The numerical algorithm is outlined in section 3.

4

The equation is put in a form suitable for ~~its resolution before~~ introducing the split-step procedure. Each step of the operator splitting is described. Section 4 deals with the analysis of the dispersion relation of the model and the influence of the numerical split-step on this dispersion relation. Details on the implementation on distributed memory architecture and the resulting performances are given in section 5. It is then validated against several test cases in section 6. Finally, it is applied to the case of the propagation of a shock wave in the planetary boundary layer (section 7) to illustrate the performances of the method.

2. Model
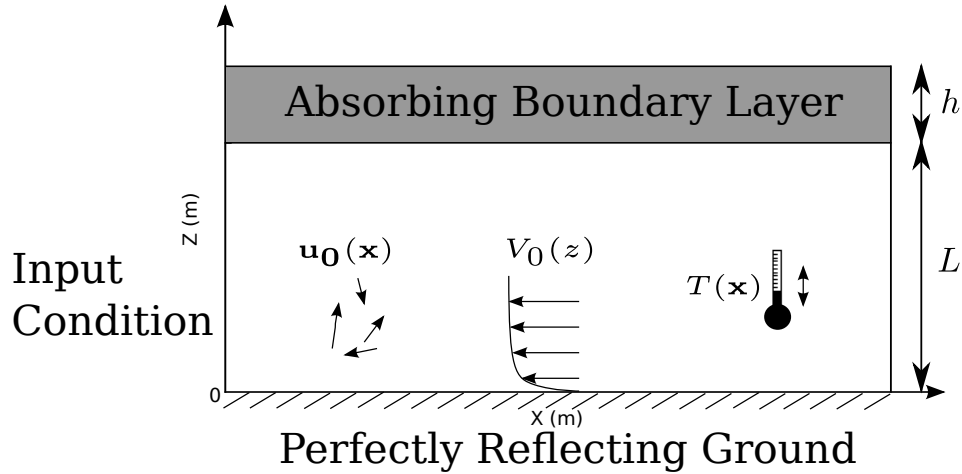
Figure 1: Schematic view of computation case for outdoor propagation over the ground.

A viscous fluid in a Cartesian domain is considered; x is the main propagation direction, z the vertical coordinate, and y the transverse one as displayed on Fig. 1. At a position $\mathbf{x}$ and time t, we denote $\rho(\mathbf{x}, t)$ the density, $c_0(\mathbf{x}, t)$ the sound speed, $\mathbf{v}(\mathbf{x}, t)$ the flow velocity, and $p(\mathbf{x}, t)$ the

5

pressure. Since the atmospheric characteristic time scales are much larger than the acoustical one (a few hours for atmospheric state, a few minutes for turbulent fluctuations and a fraction of seconds for an acoustic shock wave), the medium can be considered as frozen which means that the quantities associated with the ambient medium ($\bullet_0$) can be separated from the time varying acoustical fluctuations ($\bullet_a$):

$$f(\mathbf{x}, t) = f_0(\mathbf{x}) + f_a(\mathbf{x}, t) \tag{1}$$

with $f = (\rho, \mathbf{v}, p)$. The ambient flow is then separated between a mean vertically stratified flow $\mathbf{V_0}(z)$ with only horizontal components $\mathbf{V_0} \cdot \mathbf{e_z} = 0$, which is of order of the ambient flow Mach number M, and turbulent fluctuations $\mathbf{u_0}(\mathbf{x})$ of smaller order, *approximately M^2*:

$$\mathbf{v_0}(\mathbf{x}) = \mathbf{V_0}(z) + \mathbf{u_0}(\mathbf{x}). \tag{2}$$

This assumption is consistent with the situation in the atmospheric boundary layer where the mean wind velocity rarely exceeds 20 m/s, corresponding to a Mach number $M = \|V_0\|/c_0$ of 0.06. Its fluctuations are much lower: a few meters per second [41, 42]. Hence, the Mach number of the fluctuation is approximately of the order of $M^2 = 0.004$. Finally, the temperature fluctuations are of order 5°C to 10°C which implies that the sound speed and density fluctuations are also of the order of one percent at most and thus $O(M^2)$. Therefore they can also be separated between a mean component ($\bar{\bullet}$) and a spatially varying one ($\bullet'$):

$$c_0(\mathbf{x}) = \bar{c}_0 + c'_0(\mathbf{x}) \tag{3}$$

$$\rho_0(\mathbf{x}) = \bar{\rho}_0 + \rho'_0(\mathbf{x}). \tag{4}$$

Using these assumptions it is possible to model the nonlinear propagation of acoustic waves in a moving inhomogeneous medium with a nonlinear scalar

6

equation [43]:

$$\frac{1}{c_0^2}\frac{D_s^2 p_a}{Dt^2} - \rho_0 \mathbf{\nabla} \cdot \left(\frac{\mathbf{\nabla} p_a}{\rho_0}\right) + 2\frac{dV_{0j}}{dz}\int_{-\infty}^{t}\frac{\partial^2 p_a(\mathbf{x},t')}{\partial z \partial x_j}dt'$$

$$= -\frac{2}{c_0^2}\mathbf{u_0}\cdot\frac{\partial \mathbf{\nabla} p_a}{\partial t} + \frac{\beta}{\rho_0 c_0^4}\frac{\partial^2 p_a^2}{\partial t^2} + \frac{\delta}{c_0^4}\frac{\partial^3 p_a}{\partial t^3} \qquad (5)$$

where the operator $D_s/Dt = \partial/\partial t + \mathbf{V_0}\cdot\nabla$ is the convective derivative associated to the ambient mean flow. Eq. 5 takes into account quadratic nonlinearities and atmospheric absorption; $\beta = (\gamma+1)/2$ and $\delta = \left[\frac{4}{3}\mu + \mu_B + \kappa(c_v^{-1} - c_p^{-1})\right]/\rho_0$ are respectively the nonlinear parameter and diffusivity of the medium. Here μ is the shear viscosity, μ_b the bulk viscosity and κ the thermal conductivity, while c_p and c_v are the specific heats at constant pressure and constant volume, respectively. The ratio of the specific heats $\gamma = c_p/c_v$ is equal to 1.4 in air so that $\beta = 1.2$. Eq. 5 is of mixed order between 1 and 2 in Mach number as it contains $O(M^2)$ terms for V_{0j} in the convective derivative while neglecting the $O(M^2)$ terms corresponding with the effect of shear associated with $\frac{dV_{0j}}{dz}$. The first ones are involved in phase effects which are dominant as soon as frequency is high enough while the other ones are involved only in amplitude effects and therefore play a smaller role for the considered frequencies. These approximations are quantified numerically in [43]. The same assumption is performed on the turbulent fluctuations where all terms proportional to wind fluctuation gradients $\frac{du_{0j}}{dx_i}$ are neglected. Moreover, formally, the time derivatives associated with nonlinearities and absorption should be convective derivatives but the effect of convection can be neglected as explained in [43]. In the linear and inviscid case, Eq. 5 reduces to Eq.2.73 of Ostashev [1].

3. One-way numerical approach

3.1. Partially one-way equation

Eq. 5 is not easily handled numerically so some transformations have to be performed. First, it is written in the form of a homogeneous wave equation with a perturbation term on the right hand side:

$$\frac{1}{\bar{c_0}^2}\frac{\partial^2 p_a}{\partial t^2} - \frac{\partial^2 p_a}{\partial x^2} - \frac{\partial^2 p_a}{\partial y^2} - \frac{\partial^2 p_a}{\partial z^2} = \mathcal{P}. \tag{6}$$

The right hand side $\mathcal{P}$ contains all terms linked to flow motions, medium heterogeneities, sound absorption and nonlinearities. They all are of order M at most: $P = O(M)$.

In a second stage, in order to use a one-way propagation approach, the retarded time $\tau = t - x/\bar{c}_0$ is introduced. Eq. 6 is rewritten in a time frame moving with the mean sound speed in the x-direction.

$$\frac{2}{\bar{c_0}^2}\frac{\partial^2 p_a}{\partial x \partial \tau} - \frac{\partial^2 p_a}{\partial x^2} - \frac{\partial^2 p_a}{\partial y^2} - \frac{\partial^2 p_a}{\partial z^2} = \mathcal{P}'. \tag{7}$$

As a third step, a wide-angle parabolic approximation is applied *only* on the perturbation terms $\mathcal{P}' = O(M)$ rather than on the full wave equation 7. To achieve this, all second order derivatives in x are replaced in $\mathcal{P}'$ using the linear homogeneous equation written in retarded time:

$$\frac{\partial^2 p_a}{\partial x^2} = \frac{2}{\bar{c_0}^2}\frac{\partial^2 p_a}{\partial x \partial \tau} - \frac{\partial^2 p_a}{\partial y^2} - \frac{\partial^2 p_a}{\partial z^2} + O(M). \tag{8}$$

This wide-angle approximation is therefore of order M^2 since it is applied only on terms in $\mathcal{P}'$ that are already of order M at most. This approach is of a higher order than applying a wide-angle approximation to the full equation. As a counterpart, a second order derivative in x remains in the homogeneous part of the equation. Thus it is only a partially one-way

equation. The one-way numerical handling of this second order derivative will be dealt with in subsection 3.3. In order to handle shock waves, the acoustic pressure p_a is also replaced by the pseudo-potential:

$$p_a(\mathbf{x}) = \frac{\partial \phi}{\partial t}(\mathbf{x}). \tag{9}$$

The pseudo-potential has the advantage to remain continuous through shocks and is well adapted for the numerical treatment of the nonlinear part of the equation [14, 44]. It results finally in the following equation:

$$\frac{\partial \phi}{\partial x}(\mathbf{x}, \tau) = D\phi(\mathbf{x}, \tau) + H\phi(\mathbf{x}, \tau) + N\phi(\mathbf{x}, \tau) + A\phi(\mathbf{x}, \tau). \tag{10}$$

Operator D represents diffraction effects:

$$D\phi(\mathbf{x}, \tau) = \frac{\bar{c}_0}{2} \int_{-\infty}^{\tau} \left(\frac{\partial^2 \phi}{\partial x^2} + \frac{\partial^2 \phi}{\partial y^2} + \frac{\partial^2 \phi}{\partial z^2} \right) dt, \tag{11}$$

so that equation $\frac{\partial \phi}{\partial x}(\mathbf{x}, \tau) = D\phi(\mathbf{x}, \tau)$ is simply the usual 3D wave equation with constant sound speed $\bar{c}_0$ in a homogeneous, quiescent and non-absorbing fluid, and written in terms of retarded time τ rather than physical time t. The operator N associated to nonlinearities is:

$$N\phi(\mathbf{x}, \tau) = \frac{\beta}{2\bar{\rho}_0 \bar{c}_0{}^3} \left(\frac{\partial \phi}{\partial \tau} \right)^2. \tag{12}$$

The absorption operator A is given by:

$$A\phi(\mathbf{x}, \tau) = \frac{\delta}{2\bar{c}_0{}^3} \frac{\partial^2 \phi}{\partial \tau^2}. \tag{13}$$

Heterogeneities and wind effects are described by operator H decomposed as:

$$H\phi(\mathbf{x}, \tau) = FLH^{(1)}(\mathbf{x}, \tau) + FLH^{(2)}(\mathbf{x}, \tau) + TH(\mathbf{x}, \tau). \tag{14}$$

$FLH^{(1)}$ is the operator describing the effects of the mean vertically stratified flow $\mathbf{V}_0(z)$ on propagation. $FLH^{(2)}$ is a similar operator, but for the effects

of fully 3D turbulent fluctuations $\mathbf{u_0}(\mathbf{x})$. TH is the operator describing the influence of the medium sound speed and density inhomogeneities on the propagation. Rather lengthy expressions for these operators are found in Appendix A.

3.1.1. Simplified FLHOWARD equation

A simplified FLHOWARD equation can be written by considering only the dominant linear convection flow effects for both the mean wind and its fluctuations. Only the first line of Eq.A.1 remains. In this case, the H operator has to be replaced by $H^{(s)}$ defined as:

$$H^{(s)}\phi(\mathbf{x},\tau) = FLH^{(s)}(\mathbf{x},\tau) + TH(\mathbf{x},\tau),\tag{15}$$

with

$$FLH^{(s)}\phi(\mathbf{x},\tau) = \frac{v_{0x}}{\bar{c}_0{}^2}\frac{\partial\phi}{\partial\tau} - \frac{v_{0x}}{\bar{c}_0}\frac{\partial\phi}{\partial x} - \frac{v_{0y}}{\bar{c}_0}\frac{\partial\phi}{\partial y} - \frac{v_{0z}}{\bar{c}_0}\frac{\partial\phi}{\partial z}.\tag{16}$$

Note that for the velocity fluctuations $\mathbf{u_0}(\mathbf{x})$, operators $FLH^{(s)}$ and $FLH^{(2)}$ are identical. Operators H and $H^{(s)}$ differ only for the mean stratified flow $\mathbf{V_0}(z)$.

3.2. Split-step method

The main physical effects are clearly separated in equation 10. This is taken advantage of for the numerical split-step process. An operator splitting method is chosen [45, 46] through a spatially advancing scheme in the x-direction. It allows to solve each part of Eq. 10 separately and then to couple the solution by assembling the results. The L.H.S. is the coupling term.

$$\phi(x + \Delta x, y, z, \tau) = \phi_{\Delta x}^{D} \circ \phi_{\Delta x}^{H+A} \circ \phi_{\Delta x}^{N}(x, y, z, \tau) + O(\Delta x).\tag{17}$$

where $\circ$ is the composition operator: $g \circ f(x) = g(f(x))$ and $\phi^X_{\Delta x}$ is solution of the formal equation $\frac{\partial \phi}{\partial x}(\mathbf{x}, \tau) = X\phi(\mathbf{x}, \tau)$ over the Δx step with operator $X = D, H + A$ or N. Equation (17) is a first order split-step. For numerical reasons explained in 3.6, absorption and heterogeneities are solved during the same sub-step. Alternatively, the following second order Strang split-step [47, 45, 46] is used for higher accuracy:

$$\phi(x + \Delta x, y, z, \tau) = \phi^N_{\frac{\Delta x}{2}} \circ \phi^D_{\frac{\Delta x}{2}} \circ \phi^{H+A}_{\Delta x} \circ \phi^D_{\frac{\Delta x}{2}} \circ \phi^N_{\frac{\Delta x}{2}}(x, y, z, \tau) + O(\Delta x^2). \quad (18)$$

The main advantage of the split-step scheme is that each part of the equation is solved using an efficient numerical method adapted for each physical effect as detailed in the next three sections.

3.3. Diffraction effects

Diffraction effects are contained in the operator D defined in Eq. 11. It results into the usual wave equation (but written in terms of retarded time τ):

$$\frac{\partial \phi}{\partial x} = \frac{\bar{c}_0}{2} \int_{-\infty}^{\tau} \left(\frac{\partial^2 \phi}{\partial x^2} + \frac{\partial^2 \phi}{\partial y^2} + \frac{\partial^2 \phi}{\partial z^2} \right) d\tau'. \quad (19)$$

Eq. 19 is solved using the angular spectrum method in the spectral domain (k_y, k_z, ω) [48]. Applying Fourier transforms in retarded time and in the two transverse directions y and z, equation 19 becomes:

$$\frac{d^2 \bar{\bar{\hat{\phi}}}}{dx^2} - 2ik \frac{d\bar{\bar{\hat{\phi}}}}{dx} - \left(k_y^2 + k_z^2 \right) \bar{\bar{\hat{\phi}}} = 0 \quad (20)$$

with $k = \omega/\bar{c}_0$. Eq. 20 is a second-order linear scalar ODE with respect to advancement variable x, other variables in the spectral domain (k_y, k_z, ω) playing the role of parameters. It has two solutions: one for propagation in the positive x direction and one for the propagation in the negative x

11

direction. Only the solution propagating in the positive x direction is selected in the algorithm: *the backscattered field is canceled.* This makes the numerical solution fully one-way. If $-k^2 + \left(k_y^2 + k_z^2\right) > 0$, only the evanescent wave propagating and decaying in the positive x-direction is selected. The solution is:

$$\bar{\bar{\hat{\phi}}}(x + \Delta x, k_y, k_z, \omega) = \bar{\bar{\hat{\phi}}}(x, k_y, k_z, \omega) exp\left(\Delta x \left[ik - \sqrt{-k^2 + k_y^2 + k_z^2}\right]\right). \tag{21}$$

If $-k^2 + \left(k_y^2 + k_z^2\right) < 0$, only the wave propagating in the positive x-direction is selected. The solution is:

$$\bar{\bar{\hat{\phi}}}(x + \Delta x, k_y, k_z, \omega) = \bar{\bar{\hat{\phi}}}(x, k_y, k_z, \omega) exp\left(\Delta x \left[ik - i\sqrt{k^2 - (k_y^2 + k_z^2)}\right]\right). \tag{22}$$

The solution is then retrieved in the physical space using the inverse Fourier transforms. Practically, the Fourier transforms are implemented using Fast Fourier Transform (FFT) algorithm provided by the FFTW library [49]. This method has the advantages to be fast due to the speed of the FFT algorithm while keeping spectral accuracy.

3.4. Flows and heterogeneities effects

Heterogeneities and flows effects are contained in operator H which is rewritten as $H = H_1 + H_2$ with:

$$
\begin{aligned}
H_1 = {} & \frac{V_{0x}}{\bar{c}_0{}^2}\frac{\partial \phi}{\partial \tau} - \frac{V_{0x}}{\bar{c}_0}\frac{\partial \phi}{\partial x} - \frac{V_{0x}^2}{2\bar{c}_0{}^3}\frac{\partial \phi}{\partial \tau} + \frac{u_{0x}}{\bar{c}_0{}^2}\frac{\partial \phi}{\partial \tau} - \frac{u_{0x}}{\bar{c}_0}\frac{\partial \phi}{\partial x} \\
& + \frac{2\bar{c}_0 c_0' + c_0'^2}{2\bar{c}_0{}^3}\frac{\partial \phi}{\partial \tau} + \frac{1}{2\rho_0}\left(\frac{\partial \rho_0}{\partial x}\phi - \bar{c}_0 \int_{-\infty}^{\tau} \frac{\partial \rho_0}{\partial x}\frac{\partial \phi}{\partial x}d\tau'\right),
\end{aligned} \tag{23}
$$

and

$$
\begin{aligned}
H_2 = {} & -\frac{V_{0y}}{\bar{c}_0}\frac{\partial \phi}{\partial y} - \frac{u_{0y}}{\bar{c}_0}\frac{\partial \phi}{\partial y} - \frac{u_{0z}}{\bar{c}_0}\frac{\partial \phi}{\partial z} \\
& + \frac{V_{0x}^2}{2\bar{c}_0}\int_{-\infty}^{\tau}\left(\frac{\partial^2 \phi}{\partial y^2} + \frac{\partial^2 \phi}{\partial z^2}\right)d\tau' + \frac{V_{0x}V_{0y}}{\bar{c}_0}\left(\frac{1}{\bar{c}_0}\frac{\partial \phi}{\partial y} - \int_{-\infty}^{\tau}\frac{\partial^2 \phi}{\partial x\partial y}d\tau'\right) - \frac{V_{0y}^2}{2\bar{c}_0}\int_{-\infty}^{\tau}\frac{\partial^2 \phi}{\partial y^2}d\tau' \\
& + \bar{c}_0 V_{0x}\int_{-\infty}^{\tau}\int_{-\infty}^{\tau}\frac{\partial^3 \phi}{\partial x\partial z^2}d\tau'd\tau' - \bar{c}_0\int_{-\infty}^{\tau}\int_{-\infty}^{\tau}\frac{\partial}{\partial z}\left[V_{0x}\frac{\partial^2 \phi}{\partial x\partial z}\right]d\tau'd\tau' \\
& + \bar{c}_0 V_{0y}\int_{-\infty}^{\tau}\int_{-\infty}^{\tau}\frac{\partial^3 \phi}{\partial y\partial z^2}d\tau'd\tau' - \bar{c}_0\int_{-\infty}^{\tau}\int_{-\infty}^{\tau}\frac{\partial}{\partial z}\left[V_{0y}\frac{\partial^2 \phi}{\partial y\partial z}\right]d\tau'd\tau' \\
& + \int_{-\infty}^{\tau}\frac{d}{dz}\left[V_{0x}\frac{\partial \phi}{\partial z}\right]d\tau' - \int_{-\infty}^{\tau}V_{0x}\frac{\partial^2 \phi}{\partial z^2}d\tau' \\
& + \frac{\bar{c}_0}{2}\int_{-\infty}^{\tau}\left(\frac{\partial^2 \phi}{\partial y^2} + \frac{\partial^2 \phi}{\partial z^2}\right)d\tau' - \frac{\bar{c}_0}{2\rho_0}\int_{-\infty}^{\tau}\left(\frac{\partial}{\partial y}\left[\rho_0\frac{\partial \phi}{\partial y}\right] + \frac{\partial}{\partial z}\left[\rho_0\frac{\partial \phi}{\partial z}\right]\right)d\tau'.
\end{aligned}
$$

$$(24)$$

For a plane wave, H_1 handles the phase effects which are preponderant as long as the frequency is high enough. This is the case for the considered applications. It corresponds to the terms of Eq. 14 containing only x and τ derivatives. It is worth noting that phase effects in operator H_1 involve only: (i) convection in the main propagation direction x (the terms are linear or nonlinear with respect to V_{0x} and linear with respect to u_{0x}), (ii) sound speed heterogeneities, (iii) gradient of density in the main propagation direction. The remaining terms of Eq. 14 are contained in the operator H_2 which represents the coupling between diffraction, heterogeneities and wind for a non plane wave. Amplitude effects in operator H_2 involve: (i) linear convection due to the transverse components of the velocity field (first line), (ii) some quadratic convection terms (second line), (iii) gradient of ambient flow (lines 3 to 5), (iv) density gradients in the transverse directions (last line). The effects contained in operator H are handled in the frequency domain (ω, y, z). For stability and accuracy reasons [50], all phase effects

13

are solved analytically. The coupling of the multiple effects is achieved through a semi-implicit second order Crank-Nicolson advancement scheme.

For the simplified FLHOWARD equation, operator H_1 and H_2 are replaced by operators $H_1^{(s)}$ and $H_2^{(s)}$ defined as:

$$H_1^{(s)} = \frac{v_{0x}}{\bar{c}_0^2}\frac{\partial\phi}{\partial\tau} - \frac{v_{0x}}{\bar{c}_0}\frac{\partial\phi}{\partial x} + \frac{2\bar{c}_0 c_0' + c_0'^2}{2\bar{c}_0^3}\frac{\partial\phi}{\partial\tau} + \frac{1}{2\rho_0}\left(\frac{\partial\rho_0}{\partial x}\phi - \bar{c}_0\int_{-\infty}^{\tau}\frac{\partial\rho_0}{\partial x}\frac{\partial\phi}{\partial x}d\tau'\right),$$
(25)

$$H_2^{(s)} = -\frac{v_{0y}}{\bar{c}_0}\frac{\partial\phi}{\partial y} - \frac{v_{0z}}{\bar{c}_0}\frac{\partial\phi}{\partial z}$$
$$+ \frac{\bar{c}_0}{2}\int_{-\infty}^{\tau}\left(\frac{\partial^2\phi}{\partial y^2} + \frac{\partial^2\phi}{\partial z^2}\right)d\tau' - \frac{\bar{c}_0}{2\rho_0}\int_{-\infty}^{\tau}\left(\frac{\partial}{\partial y}\left[\rho_0\frac{\partial\phi}{\partial y}\right] + \frac{\partial}{\partial z}\left[\rho_0\frac{\partial\phi}{\partial z}\right]\right)d\tau'.$$
(26)

In this simplified case, phase effects in operator $H_1^{(s)}$ involve only: (i) linear convection in the main propagation direction x, (ii) sound speed heterogeneities, (iii) gradient of density in the main propagation direction. Amplitude effects in operator H_2 involve only: (i) linear convection due to the transverse components of the velocity field (first line), (ii) density gradients in the transverse directions.

3.4.1. Phase effects

Phase effects are defined through operator H_1 in Eq. 23 and are solved analytically. The equation to solve is:

$$\frac{\partial\phi}{\partial x} = H_1\phi.$$
(27)

In the frequency domain, it can be cast as:

$$\frac{d\hat{\phi}}{dx} = \frac{\omega^2\left[\frac{V_{0x}^2}{2\bar{c}_0^3} - \frac{V_{0x}}{\bar{c}_0^2} - \frac{u_{0x}}{\bar{c}_0^2} - \frac{2\bar{c}_0 c_0' + c_0'^2}{2\bar{c}_0^3}\right] + \frac{i\omega}{2\rho_0}\frac{\partial\rho_0}{\partial x}}{i\omega\left[1 + \frac{V_{0x}}{\bar{c}_0} + \frac{u_{0x}}{\bar{c}_0}\right] + \frac{\bar{c}_0}{2\rho_0}\frac{\partial\rho_0}{\partial x}}\hat{\phi} = \Theta(x,y,z,\omega)\hat{\phi}, \quad (28)$$

14

which is a first-order, scalar and linear ODE with respect to advancement variable x, other variables playing the role of parameters, either in the physical (y, z) or spectral (ω) spaces. Solution is given explicitly by:

$$\hat{\phi}(x + \Delta x, y, z, \omega) = \hat{\phi}(x, y, z, \omega) \exp\left(\int_x^{x+\Delta x} \Theta(\zeta, y, z, \omega) d\zeta\right). \tag{29}$$

To compute the integral, the second order trapezoidal rule (Simpson's rule) is used:

$$\hat{\phi}(x + \Delta x, y, z, \omega) = \hat{\phi}(x, y, z, \omega) \exp\left(\frac{\Delta x}{2} \left[\Theta(x) + \Theta(x + \Delta x)\right]\right) + O(\Delta x^2). \tag{30}$$

In the case of the simplified FLHOWARD equation $\Theta(x, y, z, \omega)$ is replaced by $\Theta^{(s)}(x, y, z, \omega)$:

$$\Theta^{(s)} = \frac{-\omega^2 \left[\frac{v_{0x}}{\bar{c}_0^2} + \frac{2\bar{c}_0 c_0' + c_0'^2}{2\bar{c}_0^3}\right] + \frac{i\omega}{2\rho_0} \frac{\partial \rho_0}{\partial x}}{i\omega \left[1 + \frac{v_{0x}}{\bar{c}_0}\right] + \frac{\bar{c}_0}{2\rho_0} \frac{\partial \rho_0}{\partial x}}. \tag{31}$$

3.4.2. Coupling effects

The equation $\frac{\partial \hat{\phi}}{\partial x} = H_2 \hat{\phi}$ representing the coupling between diffraction, heterogeneities and wind for a non plane wave is a 3D linear PDE of first-order with respect to advancement variable x and second-order with respect to transverse space variables (y, z). Angular frequency ω is a parameter in the spectral domain. To solve it, a semi-implicit Crank-Nicolson scheme is used in the advancement x-direction. This scheme is unconditionally stable and of second order accuracy. A second-order, centered finite difference discretization is used in the y and z directions. We resort to an Alternate Direction Implicit (ADI) method to separate the y and z directions. The two resultant matrices associated to the Crank-Nicolason scheme in each y or z directions are tridiagonal, so that they can be solved using the classical

15

Thomas' algorithm [51]. Details are given in Appendix B. The method is similar for the simplified FLHOWARD equation for operator $H_2^{(s)}$.

3.5. Nonlinear effects

The nonlinear effects are taken into account by operator N (Eq. 12) which results into the inviscid Burgers' equation:

$$\frac{\partial \phi}{\partial x} = \frac{\beta}{2\bar{\rho}_0 \bar{c}_0^3} \left(\frac{\partial \phi}{\partial \tau}\right)^2,$$ (32)

which is a first-order two-dimensional scalar PDE with respect to variables x and τ, other space variables (y, z) playing the role of parameters. To solve it, the quasi-analytical Burgers-Hayes methods is chosen. It relies on the implicit Poisson solution. Poisson solution is exact as long as it is single-valued (no shock). In case of a multi-valued solution (beyond the shock formation), the weak shock theory is used. Burgers-Hayes method [52, 14, 44] handles it in a very efficient numerical way using the fact that the physical solution for the potential corresponds to the *maximum* value of the multivalued Poisson's solution. This condition is necessary to satisfy the second principle of thermodynamics:

$$
\begin{aligned}
\phi(x, y, z, \tau) &= max \left[\phi(x, y, z, \theta) - \frac{\beta \Delta x}{\bar{\rho}_0 \bar{c}_0^3} \left(\frac{\partial \phi(x, y, z, \theta)}{\partial \theta} \right) \right] \\
\tau &= \theta - \frac{\beta \Delta x}{\bar{\rho}_0 \bar{c}_0^3} \frac{\partial \phi(x, y, z, \theta)}{\partial \theta}.
\end{aligned}
$$ (33)

A numerical interpolation is needed to retrieve the solution Eq. 33 on the initial retarded time τ grid. Practically, the order of this interpolation makes no differences, thus only a first order interpolation is used.

3.6. Absorption and relaxation

Operator A deals with the absorption of the medium. In the atmosphere, at audible frequencies or below, the thermoviscous absorption included in

16

Eq. 13 is not the main attenuation mechanism. Dominant absorption terms are due to relaxation of molecular nitrogen and oxygen and is controlled by the water vapour content [53, 54, 55, 15]. Thus an ad-hoc expression is added to include attenuation and dispersion due to relaxation:

$$\frac{d\phi}{dx} = L_\tau(\phi). \tag{34}$$

L_τ is a linear operator containing the effects of attenuation and dispersion in a thermoviscous fluids containing multiple relaxation mechanisms. It is given by:

$$L_\tau(\phi) = \frac{\delta}{2\bar{c}_0^3} \frac{\partial^2 \phi}{\partial \tau^2} + \sum_j \frac{c_j'}{\bar{c}_0^2} \int_{-\infty}^\tau \frac{\partial^2 \phi}{\partial \tau'^2} e^{-(\tau-\tau')/t_j} d\tau' \tag{35}$$

with δ the diffusivity of sound defined by Eq. 2, t_j the relaxing time of the jth relaxation process and c_j' the increase in phase velocity associated with this mechanism when the frequency goes from 0 to infinity.

Eq. 34 is solved analytically in the frequency domain in the same manner as for the phase effects of heterogeneous and flow terms (operator H_1):

$$\hat{\phi}(x + \Delta x, y, z, \omega) = \hat{\phi}(x, y, z, \omega) \exp\left[\left(-\frac{\omega^2 \delta}{2\bar{c}_0^3} - \frac{\omega}{\bar{c}_0^2} \sum_j \frac{c_j' \omega t_j}{1 + i\omega t_j}\right) \Delta x\right]. \tag{36}$$

Practically, this absorption substep is integrated in the same advancement step as H_1 to limit the computation time. Details on the absorption coefficients in the atmosphere can be found in [56].

3.7. Boundary conditions

The code is designed to perform simulations of acoustic propagation in the atmosphere near the ground (Fig. 1). Hence, at least two kinds of boundary conditions are required. The perfectly rigid ground is modeled

17

using a perfectly reflecting boundary condition. The other boundary conditions are handled as artificial absorbing layers mimicking infinite medium in the vertical ($z > 0$) and lateral (y) directions.

3.7.1. Reflecting boundary conditions

The perfectly rigid condition is:

$$\left.\frac{\partial p_a}{\partial z}\right|_{z=0} = 0. \tag{37}$$

The difficulty to implement this boundary condition comes from the use of Fourier transforms to solve the diffraction operator. The classical discrete Fourier transform enforces periodicity on the boundaries. The simplest way to take into account this boundary conditions is the image method [57] which consists in solving the symmetric problem of the one we are solving. However, it is numerically inefficient both in terms of computation time and of memory usage since one has to solve the problem on a domain twice as big as needed. This solution was previously implemented in FLHOWARD 2D [40] but is not tractable in 3D due to the memory that would be required. Another common solution is to solve the problem on a grid generated by using Chebyshev or Legendre polynomials [58]. With this method, the grid is no longer Cartesian, which is more complicated to implement. To overcome this problem, FLHOWARD3D uses the cosine transform to enforce von Neumann boundary condition (Eq. 37):

$$\bar{\phi}(y, k_z, \tau) = \int_{-\infty}^{\infty} \phi(y, z, \tau) \cos(ik_z z) dz. \tag{38}$$

Discrete Cosine Transform (DCT) naturally enforces even parity at both of its extremities [49] and can be computed efficiently using FFTW. Another advantage is that Dirichlet boundary condition $p_a(z = 0) = 0$ can also be

modeled using the Sine transform. Also, combination of Cosine and Sine transform should allow us to extend this work to the propagation over a finite impedance ground as it has been done in electromagnetism [59].

3.7.2. Absorbing boundary layer

The current state of the art for enforcing non reflecting boundary conditions is the Perfectly Matched Layers (PML) [60, 61]. With PML, waves arriving on a boundary with any incidence angle will not reflect. Instead of PML, the simpler Absorbing Boundary Layer (ABL) reduces the reflection on the border of the domain. It consists in introducing an artificial absorption term in an upper layer in order to absorb the incident wave as shown on Fig. 1. This artificial absorption term is implemented in addition to the physical absorption. The absorption coefficient is quadratically increasing from the beginning of the layer to the upper domain limit. It is the same as implemented in FLHOWARD2D [38, 50]:

$$\widehat{\phi}(x + \Delta x, y, z, \omega) = \widehat{\phi}(x, y, z, \omega) \exp\left(-\alpha(z)\Delta x\right) \tag{39}$$

with

$$\alpha(z) == \begin{cases} 21\dfrac{(z-L)^2}{h^3} \text{ if } L < z < L + h, \\ 0 \text{ else,} \end{cases} \tag{40}$$

where L is the height of the physical domain and h is the height of the ABL.

3.8. Synthesis

The overall numerical scheme is synthesized in Table 1. For the sake of simplicity, the table shows only the succession of numerical operations for the first-order Strang splitting. Changes from physical variables (y, z, τ) to spectral variables (k_y, k_z, ω) are indicated by FFT lines. For each physical

19

effect, each Ordinary or Partial Differential Equations to be solved is recalled along with its corresponding independent variables. Other variables play the role of known parameters. In each case, the numerical method and its order of approximation are also indicated. FFT operations all have a spectral precision. Other numerical operators are of order 2. For the analytical solution of nonlinear effects, the only numerical operation is the interpolation of the nonlinearly distorted retarded time mesh on the initial one, which can be done at first or second order. Though in theory a second order interpolation would keep the overall precision of the algorithm, no difference could be observed when using a first order only interpolation.

4. Numerical analysis: dispersion relations

4.1. Model equation

The validity of the model (Eq. 10) for a linear propagation, when operators $N\phi(\mathbf{x})$ and $A\phi(\mathbf{x})$ are set to zero, can be examined precisely by writing its dispersion relation for a bi-dimensional plane wave:

$$\phi(x, z, \tau) = \phi_0 \exp \left[i k_0 \left((\bar{k}_x - 1)x + \bar{k}_z z - \bar{c}_0 \tau \right) \right] \tag{41}$$

where $k_0 = \omega_0 / \bar{c}_0$ is the wave number, and $\bar{k}_x = k_x / k_0$, $\bar{k}_z = k_z / k_0$ are the dimensionless components of the wave vector. The investigated case is the propagation of a plane wave in a uniform flow parallel to the selected direction Ox of propagation ($V_{0x} = cte$, $V_{0y} = 0$). The exact convected wave equation in this case is given by:

$$\frac{D_s^2 p_a}{Dt^2} - c_0^2 \Delta p_a = 0, \tag{42}$$

which corresponds to the dispersion relation:

$$\bar{k}_x^2 + \frac{2M}{1 - M^2} \bar{k}_x + \frac{\bar{k}_z^2 - 1}{1 - M^2} = 0. \tag{43}$$

20

Physical Effect(s)	Sub-equation (NATURE)	Numerical variables [Parameters]	Method	Order
3D FFT		$(x,y,z,\tau) \downarrow$ (x,k_y,k_z,ω)		SP
Diffraction (homogeneous wave Eq.)	$\frac{d\bar{\bar{\hat{\phi}}}}{dx} = D\bar{\bar{\hat{\phi}}}$ (ODE)	x $[k_x,k_y,\omega]$	Analytical Eqs.(21-22) but backscatterng neglected	2
2D FFT		$(x,k_x,k_y,\omega) \downarrow$ (x,y,z,ω)		SP
Heterogeneities (phase effects) + Absorption	$\frac{d\hat{\phi}}{dx} = (H_1 + L_\tau)\hat{\phi}$ (ODE)	x $[y,z,\omega]$	Analytical Eq.(29) + 2nd order Simpson rule Eq.(30)	2
Heterogeneities (coupling effects) (optional)	$\frac{\partial \hat{\phi}}{\partial x} = H_2\hat{\phi}$ (3D PDE)	(x,y,z) $[\omega]$	ADI Δx : Crank-Nicolson $\Delta y, \Delta z$: centered FD	2
1D FFT		$(x,y,z,\omega) \downarrow$ (x,y,z,τ)		SP
Nonlinearities	$\frac{\partial \phi}{\partial x} = N\phi$ (2D PDE)	(x,τ) $[y,z]$	Semi-analytical Eq.(33)	1 or 2

Table 1: Synthesis of numerical method. SP : Spectral Precision - ODE : Ordinary Differential Equation - PDE : Partial Differential Equation - ADI : Alternate Direction Implicit - FD : Finite Differences

Flhoward equation for $FLH^{(1)}$ (in this case $FLH^{(2)} = 0$) is written:

$$\frac{\partial \phi}{\partial x} = \frac{\bar{c}_0}{2} \int_{-\infty}^{\tau} \left(\frac{\partial^2 \phi}{\partial x^2} + \frac{\partial^2 \phi}{\partial z^2} \right) d\tau' + \frac{V_{0x}}{\bar{c}_0^2} \frac{\partial \phi}{\partial \tau} - \frac{V_{0x}}{\bar{c}_0} \frac{\partial \phi}{\partial x} + \frac{V_{0x}^2}{2\bar{c}_0} \left(\int_{-\infty}^{\tau} \frac{\partial^2 \phi}{\partial y^2} d\tau' - \frac{1}{\bar{c}_0^2} \frac{\partial \phi}{\partial \tau} \right),$$
$$(44)$$

and its associated dispersion relation is:

$$\bar{k}_{x\,FLH^{(1)}}^2 + 2M\bar{k}_{x\,FLH^{(1)}} + \left(\bar{k}_z^2 - 1 \right)\left(1 + M^2 \right) = 0. \qquad (45)$$

Equations 43 and 45 differ only by a term of order $O(M^3)$ which is consistent with the assumption made in establishing Eq. 10. To obtain a higher order

of precision, the Mach number M can be replaced by $M/\left(1-M^2\right)$. The difference between the two dispersion relations then becomes of order $O(M^4)$ [40, 50]. The lower order FLHOWARD equation for $FLH^{(s)}$:

$$\frac{\partial\phi}{\partial x} = \frac{\bar{c}_0}{2}\int_{-\infty}^{\tau}\left(\frac{\partial^2\phi}{\partial x^2}+\frac{\partial^2\phi}{\partial z^2}\right)d\tau' + \frac{V_{0x}}{\bar{c}_0{}^2}\frac{\partial\phi}{\partial\tau} - \frac{V_{0x}}{\bar{c}_0}\frac{\partial\phi}{\partial x} \tag{46}$$

has the dispersion relation:

$$\bar{k}_{x\,FLH^{(s)}}^{\,2} + 2M\bar{k}_{x\,FLH^{(s)}} + \left(\bar{k}_z^{\,2}-1\right) = 0, \tag{47}$$

which clearly differs from Eq. 43 by terms of order M^2. Finally, the last equation to compare is the parabolic equation of Averyianov *et al.* [35, 34, 62]:

$$\frac{\partial\phi}{\partial x} = \frac{\bar{c}_0}{2}\int_{-\infty}^{\tau}\frac{\partial^2\phi}{\partial z^2}d\tau' + \frac{V_{0x}}{\bar{c}_0{}^2}\frac{\partial\phi}{\partial\tau}, \tag{48}$$

which leads to the dispersion relation:

$$\left(\bar{k}_{x\,PE}-1\right) + M + \frac{\bar{k}_z^{\,2}}{2} = 0. \tag{49}$$

On Fig. 2, the various dispersion relations are compared for $M = 0.1$, $M = 0.3$ and $M = 0.5$. First, contrary to the parabolic approximation, the dispersion relations for the two FLHOWARD methods (full and simplified) are not one way, since the one way approximation is only performed during the numerical process. The dispersion relation for the full FLHOWARD equation with $FLH^{(1)}$ is computed with M replaced by $M/(1-M^2)$ to get the high order accuracy as visible on the figure. However, simplified FLHOWARD equation with $FLH^{(s)}$ is also more accurate than the classical parabolic equation. The improvement is due mostly to the diffraction term $\frac{\partial^2\phi}{\partial x^2}$ rather than the higher order flow terms, especially in case of low Mach numbers, since there are only small differences between $FLH^{(1)}$ and $FLH^{(s)}$. It is to be noted that both approximations behave really well even with

22

relatively high Mach number (here $M = 0.5$ is much larger than realistic atmospheric values), even if the Mach number is supposed to be small for the derivation of the equations.

4.2. Influence of the split-step method

On Sec. 4.1, the dispersion relation of Eq. 10 was examined. This did not take into account the effect of the numerical split-step process. Here, the effect of the split-step method on the dispersion relation is investigated. As was done in 4.1, a plane wave solution under the form of Eq. 41 is injected in the studied equation. First, for the angular spectrum method associated to operator D:

$$\frac{\partial^2 \phi}{\partial x \partial \tau} = \frac{\bar{c}_0}{2} \left(\frac{\partial^2 \phi}{\partial x^2} + \frac{\partial^2 \phi}{\partial y^2} + \frac{\partial^2 \phi}{\partial z^2} \right), \tag{50}$$

as backward propagation is not included, one gets:

$$\bar{k}_{x1} = \sqrt{1 - \bar{k}_z^2}. \tag{51}$$

Then equation associated to operator $FLH^{(1)}$ reduces to:

$$\frac{\partial^2 \phi}{\partial x \partial \tau} = \frac{V_{0x}}{\bar{c}_0^2} \frac{\partial^2 \phi}{\partial \tau^2} - \frac{V_{0x}}{\bar{c}_0} \frac{\partial^2 \phi}{\partial x \partial \tau} + \frac{V_{0x}^2}{2\bar{c}_0} \left(\frac{\partial^2 \phi}{\partial z^2} - \frac{1}{\bar{c}_0^2} \frac{\partial^2 \phi}{\partial \tau^2} \right). \tag{52}$$

Its dispersion relation is:

$$\bar{k}_{x2} = \frac{1}{1 + M} \left(1 - \frac{M^2}{2} \left(\bar{k}_z^2 + 1 \right) \right). \tag{53}$$

The total dispersion relation for the split-step method is given by:

$$\bar{k}_{xFLH_{num}^{(1)}} = \sqrt{1 - \bar{k}_z^2} + \frac{1}{1 + M} \left(1 - \frac{M^2}{2} \left(\bar{k}_z^2 + 1 \right) \right) - 1. \tag{54}$$

Similarly, for the operators D and $FLH^{(s)}$, we get:

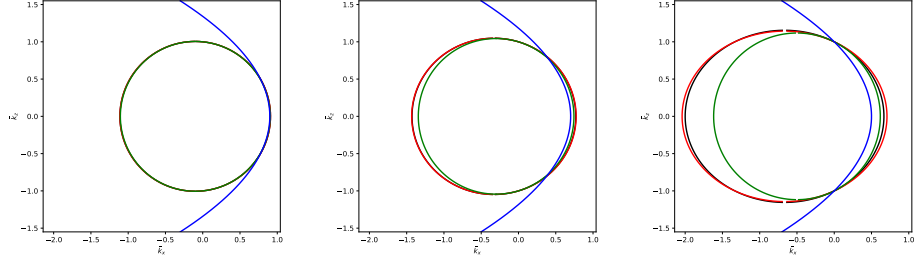$$\bar{k}_{xFLH_{num}^{(s)}} = \sqrt{1 - \bar{k}_z^2} + \frac{1}{1 + M} - 1. \tag{55}$$

23

Figure 2: Dispersion relations for the exact solution at $M = 0.1$ (left), $M = 0.3$ (middle), and $M = 0.5$ (right). Black: convected wave equation; red: full FLHOWARD equation with $FLH^{(1)}$; green: simplified FLHOWARD equation with $FLH^{(s)}$; blue: standard parabolic approximation.

As was done in 4.1 a comparison is made with the parabolic approximation of Averyianov (Eq. 48) whose dispersion relation is unaffected by the split-step method since it involves only first order effects which are completely uncoupled.

On Fig. 3, the dispersion relation for the FLHOWARD method is now one way. Some discrepancies with the exact case appear for all wave numbers for $FLH^{(1)}$ while, surprisingly, only propagation at large angles induces an error for $FLH^{(s)}$. So in the present numerical method, adding higher order terms leads to an increased dispersion error for the case of a uniform flow. For comparison, the parabolic equation has, for the same range of Mach numbers, a good accuracy only for small angles of propagation.

To better understand why $FLH^{(1)}$ induces a larger error at large Mach numbers, a Taylor expansion with respect to Mach number M up to order $O(M^3)$ is performed on the above numerical dispersion relations. They become:

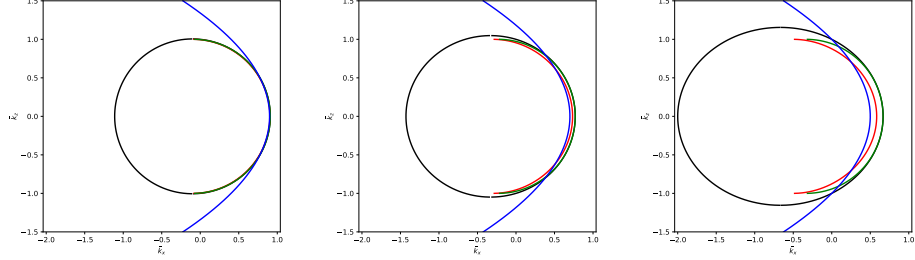- for the exact convected wave equation:

24

Figure 3: Dispersion relations for the split step numerical solution at $M = 0.1$ (left), $M = 0.3$ (middle), and $M = 0.5$ (right). Black: convected wave equation; red: full FL-HOWARD equation with $FLH^{(1)}$; green: simplified FLHOWARD equation with $FLH^{(s)}$; blue: standard parabolic approximation.

$$\bar{k}_x = \sqrt{1 - \bar{k}_z^{\,2}} - M + M^2 \left(\sqrt{1 - \bar{k}_z^{\,2}} + \frac{1}{2} \frac{\bar{k}_z^{\,2}}{\sqrt{1 - \bar{k}_z^{\,2}}} \right) + O(M^3); \quad (56)$$

- for FLHOWARD with full operator $FLH^{(1)}$:

$$\bar{k}_{xFLH_{num}^{(1)}} = \sqrt{1 - \bar{k}_z^{\,2}} - M + \frac{M^2}{2} \left(1 - \bar{k}_z^{\,2} \right) + O(M^3); \quad (57)$$

- for FLHOWARD with simplified operator $FLH^{(s)}$:

$$\bar{k}_{xFLH^{(s)}num} = \sqrt{1 - \bar{k}_z^{\,2}} - M + M^2 + O(M^3); \quad (58)$$

- for Averiyanov parabolic equation:

$$\bar{k}_{xPE} = 1 - \frac{\bar{k}_z^{\,2}}{2} - M + O(M^3). \quad (59)$$

The first three ones are strictly identical up to order M thanks to the angular spectrum method. As expected, parabolic equation is valid only for small angles of propagation. At second order M^2, due to the combined effects of equation approximations *and* numerical split step, the $FLH^{(1)}$ operator induces a systematic error of order M^2 even for small angles of propagation

when $\bar{k}_z << 1$. On the contrary, the $FLH^{(s)}$ turns out to be precise up to order $M^2 \bar{k}_z^4$. Therefore it remains much more accurate as long as $\bar{k}_z$ is not too large.

Consequently, this analysis proves the use of FLHOWARD equation with simplified operator $FLH^{(s)}$ is recommended. This is due to the *numerical* split-step method, combined with the underlying approximations of the FLHOWARD equation.

5. Parallel computing and performance test

Three dimensional computations require parallelization of the algorithm. For an acoustic wave at a frequency $f_0 = 10$ Hz in a domain $(x, y, z) = (3 \times 3 \times 3 \ km^3)$ using ten points per wavelength, we have $\delta x = 3.4$ m. It means that around one thousand points in each directions are required. Around the same number of points is needed for the temporal discretization. Thus the problem has about 10^{12} degrees of freedom. Distributed memory computers have many processors, each with its own memory. They allow to tackle bigger computations with the restitution time remaining acceptable. Currently, this kind of computation is classical and finite-differences, finite-elements or finite-volumes codes implement it. The domain can be decomposed so as to allocate one sub domain to one processor which performs its computations on this small part of the numerical domain. It is also known as the Single Program Multiple Data (SPMD) paradigm. However, here, this strategy is complicated due to the presence of Fourier transforms in the algorithm. A Fourier transform is a non-local operation incompatible with the SPMD paradigm. To handle this, the 1D decomposition (also known as slab decomposition) is implemented. The domain is only decom-

posed in one direction, the two others remaining local to the processor. With this method the Fourier transform can be applied on two directions. For the last direction, a parallel transpose is done so that the decomposed direction is changed. This parallel transpose requires a lot of data to be transferred between the processors: it is an MPI_ALL_TO_ALL instruction, which means that each processor broadcasts the data to the others. There exist alternative strategies such as 2D pencils which consist in a 2D decomposition of the domain. Pencils are efficient if the number of cores is greater than the smallest number of points amont Ny, Nz, Nt [63], otherwise 1D slab decomposition is more efficient (where Ny, Nz, Nt are respectively the number of points in the $y-$, $z-$ and $t-$ directions). For the moment, the 1D slab decomposition has been chosen here as, for our target applications, the typical values are $(Ny, Nz, Nt) = (1024, 1024, 1024)$ or more. Nevertheless, 2D pencils could be implemented in the future if the number of cores becomes an issue. Indeed this would be compatible with the other steps of the method. Practically, the 1D decomposition is implemented thanks again to the FFTW library which provides FFT and DCT operators, and parallel transposition [49].

Two metrics are used to quantify the code performances. The first one is the strong scaling. It is defined as how the restitution time varies with the number of processors for a fixed overall problem size. Ideally, the restitution time should be halved when doubling the number of cores. Strong scaling is a measure needed when the goal is to tackle a problem quicker when using more computational cores *i.e.* for cpu-bound computation. The second one is weak scaling. It is defined as how the restitution time varies with the number of processors for a fixed problem size *per processor*. Ideally, the restitution time should remain constant when both the mesh number of

points and the number of cores are doubled. It is of interest when a bigger mesh is needed, i.e. for memory-bound computations.

These performances tests are performed on the cluster of Institut Jean le Rond d'Alembert (UMR7190 UPMC CNRS) which has 29 nodes of four 6-cores (AMD Opteron 2435 processors) cadenced at 2.6 GHz for a total of 696 cores. Its theoretical peak processing power is 3 Tflops. Each node has 64 GB of memory resulting in a total of 1,8 TB of RAM for the entire cluster. The nodes are interconnected with Infiniband connections. The operating system is a Linux CentOS. The procedure used is the following. We simulate the propagation of an N-wave of amplitude 100 Pa and duration 0.2 s through an acoustical lens resulting from a 3D sound speed heterogeneity. Such a test case has already been selected [38] for mesh convergence studies at 2D. The reader is refereed to this reference for details about the speed heterogeneity. It is here chosen because it involves all the main operators D, N and H_1 of the algorithm. All the writing and reading operations on the hard-disk are deactivated so as to quantify only the computation efficiency in the test. The results are presented in time spent for performing one advancement step from x to $x + \Delta x$. To compute this, hundred steps are performed and the computational time is divided by 100 for averaging in order to reduce the errors of measurement.

Strong scaling:. For the strong scaling, two configurations were tested. The first one has a domain $(N_\tau \times N_y \times N_z)$ of $(1024 \times 1024 \times 1024)$ resulting in 1 billion points while the second one has 4 billions points with a domain of $(2048 \times 2048 \times 1024)$. These two domain sizes were chosen because they are the targeted domain sizes for the code applications. Computations were performed on up to 512 cores. Results presented on Fig. 4 show a good

28

strong scaling with a 1.7 decrease in computation time when doubling the number of cores, compared to the ideal linear case of factor 2. For these sizes of mesh, the computation cost is mostly communications between cores even using MPI_ALL_TO_ALL calls. Let us recall that such a collective communication instruction is requested here only for transposition operations as explained in section 5. The change in slope between 16 (where the slope is almost 2) and 32 cores for the smallest domain occurs because, for 16 cores, only one node is necessary, whereas for more than 24 cores several nodes are used. Then communications are no longer local to the node and use the Infiniband network.

Weak scaling:. During the weak scaling test, three different numbers of points per core were tested: 2^{20}, 2^{22} and 2^{24}. They correspond respectively to a domain size $(N_\tau \times N_y \times N_z)$ of $(64 \times 128 \times 128)$, $(256 \times 128 \times 128)$ or $(256 \times 256 \times 256)$ points per core. Computations were performed using from 8 up to 512 cores. Good overall weak scaling is achieved as can be seen on Fig. 4. The restitution time increases by a factor around 2 only, while the overall domain size and number of cores increase by a factor 64. As expected, the performance for the domain of smallest size (2^{20} points per core) is not as good (factor 2.4) as for the domains of bigger size (factor 1.8). This is because, for a small number of points, communications between cores become more important in the restitution time.

For both weak and strong scaling, the results do not depend on the specific value of N_τ, N_y or N_z but only on the overall number of points $(N_\tau \times N_y \times N_z)$. The parallelization strategy therefore seems to show good results for the considered applications which target domain sizes of the order of a few billions points distributed on around typically 256 cores.
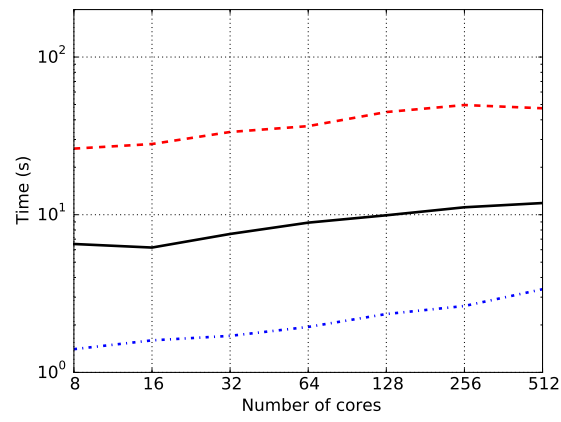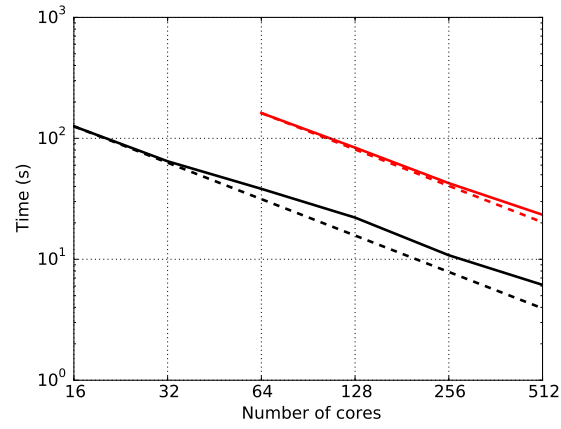
29

Figure 4: Left: strong scaling. ——— domain $(1024 \times 1024 \times 1024)$, ———: domain $(2048 \times 2048 \times 1024)$, dashed lines: linear scaling. Right: Weak scaling. — — —: 2^{20}, ——— 2^{22}, — — —: 2^{24} points per core.

6. Some validation cases

6.1. Three-dimensional circular acoustic piston in a linear homogeneous medium

The first validation test addresses the 3D propagation of a pure tone wave in a linear homogeneous medium. It is chosen to validate at 3D the diffraction part (operator D) of the algorithm along with the efficiency of the Absorbing Boundary Layer (ABL). The case of a circular piston in three-dimensions is considered. The analytical solution of this problem [57, 15] is given in Appendix C. Note that the name piston is somewhat inappropriate in this case since pressure is imposed on the surface whereas for a true piston the velocity would be imposed. For the classical parabolic equation it would be meaningless to make the difference, but for higher-order methods such as FLHOWARD, it is not equivalent. The parameters are chosen to correspond to high-intensity focused ultrasound (HIFU) treatment: $c_0 = 1500$ m/s, $\rho_0 = 1000$ kg/m^3. The incident wave is sinusoidal with a frequency $f = 1$ MHz and a wavelength $\lambda = 0.0015$ m. The radius of the piston is $r = 0.006$ m which corresponds to 4λ. A uniform pressure of 5 Pa is applied on this surface and the pressure is set to zero outside. The computational domain extends from 0 m to 0.25m (0 to 250λ) in the propagation direction (x), -0.07 m to 0.07m $(-33\lambda$ to $33\lambda)$ in the transverse directions (y, z) and from 0 s to 10^{-6} s (one period) in time. Numerically, each direction (x, y, z, τ) is discretized using 1024 points. Therefore the problem has 10^{12} degrees of freedom. Absorbing boundary layers of size 0.02 m are used so that the physical domain is reduced to -0.05 m to 0.05 m in the transverse directions.

Fig. 5 (top) shows the pressure amplitude radiated by the piston in the (x, y) plane where the characteristic diffraction pattern can be seen. The
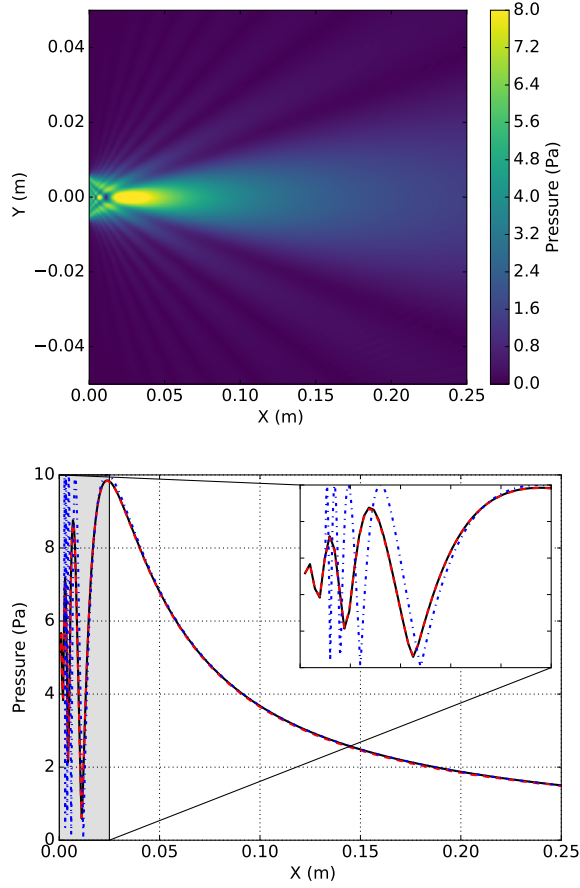
Figure 5: Left: pressure amplitude (in Pa - Color level) radiated by a pure tone pressure piston. Right: pressure amplitude on the axis of a 3D pressure piston. ——————FLHOWARD computation, — — — Analytical solution and — - — Analytical solution for the parabolic equation. The near-field is zoomed.

comparison with the analytical solution on the x-axis in Fig. 5 (bottom) shows a perfect agreement even in the near-field, a zone which is poorly reproduced by the parabolic approach. These results show the ability of the method to simulate the propagation in a homogeneous free field. Note that

the lateral absorbing boundary layers play a key role. Indeed, their presence kills reflections on the boundaries of the computational domain. Simulations without ABLs (not shown here) would show spurious oscillations appearing and would highly degrade the quality of the solution.

6.2. Scattering of a plane wave by a a spherical heterogeneity

The scattering of a plane wave by a discontinuous 3D spherical heterogeneity in sound speed is now investigated. The only two physical effects present are the heterogeneous part (operator TH) coupled with the diffraction (operator D). This problem has an analytical solution [64] [57] described in Appendix C. The physical parameters are chosen to correspond to sonic boom propagation through the atmosphere. However the intensity of the heterogeneity is chosen intentionally much larger than what could be encountered in the atmosphere. The medium celerity and density are respectively $c_0 = 340$ m/s and $\rho_0 = 1.2\ kg/m^3$. The incident plane wave has an amplitude of 100 Pa and a frequency of $f = 5$ Hz which corresponds to a wavelength $\lambda = 68$ m. The heterogeneity is a sphere placed at the center of the domain. Its radius is $r = 68$ m, equal to one wavelength. The sound speed in the sphere is $c_h = c_0(1 + 0.05)$ m/s corresponding to a uniform 5 % increase. The computational domain extends from 0 m to 1020 m (0 to 15λ) in the propagation direction (x), -2040 m to 2040 m (-30λ to 30λ) in the transverse directions $(y$ and $z)$ and from 0 s to 0.2 s (one period) in time. Numerically, each direction $(x,\ y,\ z,\ \tau)$ is discretized using 1024 points. Reflecting boundary conditions are used. They are far enough from the heterogeneity so as not to interfere with the transmitted field in the considered domain. This case is much more demanding than the atmospheric application the model was designed for. First the heterogeneity is discon-

33

tinuous whereas the parameters of the atmosphere are varying continuously. Second, the intensity of the heterogeneity, 5% in sound speed, corresponds to a variation of temperature of 34° C, extremely large for the atmosphere over such a short distance.

Fig. 6 shows the pressure amplitude scattered by the heterogeneity in the (x, y) plane. We can see the characteristic diffraction pattern. Comparison with the analytical results in Fig. 6 shows good agreement. The main differences are: (i) the amplitude value of the low pressure just after the heterogeneity in the defocusing zone, (ii) the lack of oscillations before the heterogeneity in our result. The difference of amplitude in the defocusing area is dependant on the number of points used and full convergence is hard to achieve. This is probably due to the difficulty of meshing properly a sphere with a cartesian grid. Note that the position of the minimum is well reproduced. The absence of oscillations is due to the one-way approach, as the backscattered wave is numerically not taken into account. The hypothesis of negligible backscattering thus appears acceptable if the heterogeneity is small (less than 5 %) in sound speed contrast.

6.3. Nonlinear propagation in a thermoviscous medium

To validate the nonlinear and absorption part, we use the 1D case of propagation of a pure tone acoustic wave of angular frequency ω_0 in a nonlinear thermoviscous medium. This problem has an analytical solution given by Mendousse [53]. The parameters controlling this case are $P = p_a/P_0$ the acoustical pressure normalized by the pressure amplitude at the source P_0, $X = \frac{\sigma \rho_0 c_0}{\beta P_0 \omega_0}$ the propagation distance, $\alpha = \frac{\beta P_0 \omega_0}{\Gamma \rho_0 c_0^3}$ the absorption coefficient and $\Gamma = \frac{\beta P_0 \omega_0}{\alpha \rho_0 c_0^3}$ the Gold'berg number which measures the ratio between nonlinearity and absorption. Notation σ is for the dimensionless distance
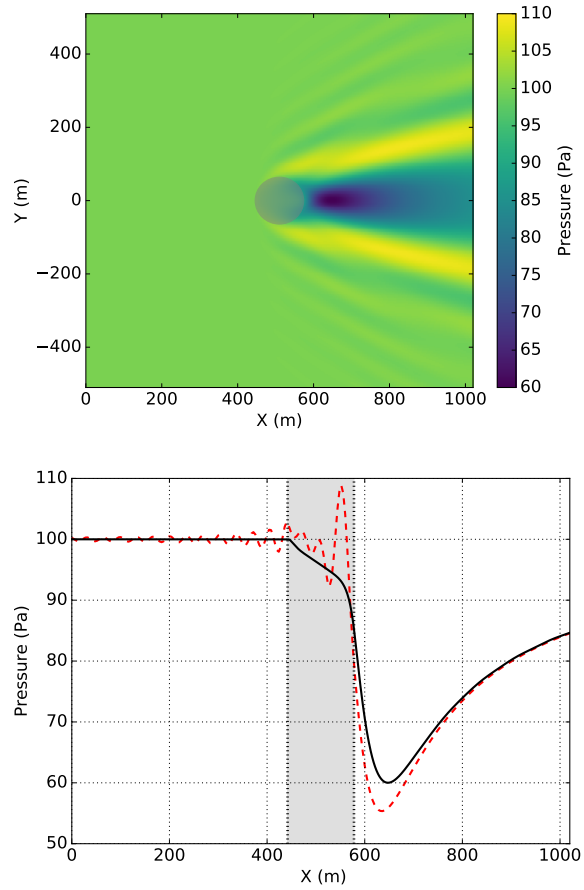
34

Figure 6: Left: pressure amplitude (in Pa - Color level) resulting from scattering of a plane wave by a heterogeneous sphere. The gray zone marks the heterogeneity location. Right: axial pressure amplitude resulting from scattering of a plane wave by a heterogeneous sphere. ———— FLHOWARD, ‒ ‒ ‒ Analytical. The grey zone marks the heterogeneity location.

and $\sigma = 1$ corresponds to the shock formation distance in the inviscid case. Here, the parameters are chosen to be $\Gamma = 50$ and $\sigma = 3$ so that the final point is well beyond the shock distance and the shock wave is well formed with a characteristic saw-tooth shape. The large Gold'berg number implies that the primary effect is the nonlinearity which strongly dominates over the absorption. Numerically 512 points are used to discretize the waveform in retarded time.

Fig. 7 shows the waveform at $\sigma = 3$ using 200 points in the $x-$direction. FLHOWARD results and the analytical solution are indiscernible. The same conclusion is drawn when examining the wave spectrum up to 60th harmonics on Fig 7. The least-square error metric defined by:

$$error_\% = 100 \frac{\sum\limits_{N_\tau} [P_{FLHOWARD}(\tau) - P(\tau)]^2}{\sum\limits_{N_\tau} P(\tau)^2} \qquad (60)$$

is plotted against the number of discretization points in the axial direction N_x used for propagation in Fig. 8. The error remains small, even if a small number of points is used for the propagation. As expected [5], the second order split-step induces a great improvement compared to the first order split step: the error is nearly always under 1%, even for a very small number of points (as soon as N_x is larger than 20, which is equivalent to say that an error less than 1% is achieved with 7 points per shock formation distance). Note that the error curves saturate for a large number of points, because round-off errors contaminate the numerical evaluation of the analytical solution (Eq. C.8), for simultaneously a large index (n) and a large argument $(\Gamma/2)$ of the modified Bessel function.
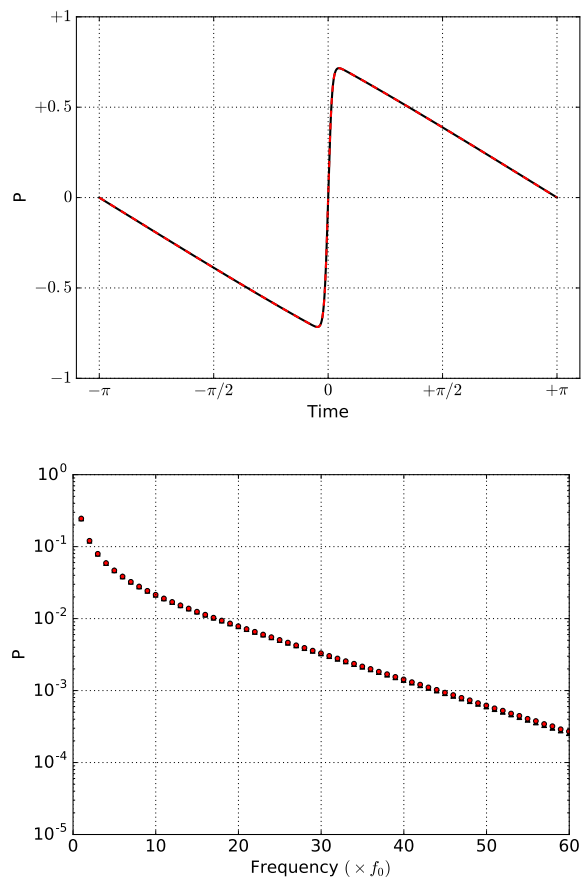
Figure 7: Left: pressure amplitude for the propagation of a plane wave in a nonlinear thermoviscous medium. Right: pressure amplitude of the first 60 harmonics for the propagation of a plane wave in a nonlinear thermoviscous medium. ———FLHOWARD, – – – Analytical.
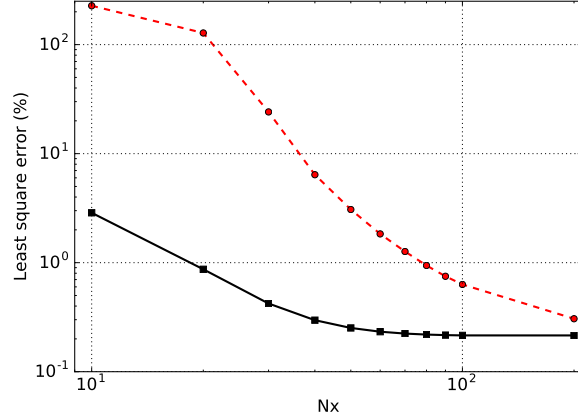
Figure 8: Effect of the split-step and discretization (N_x number of discretization points in the propagation direction) on the error for the propagation of a plane wave in a nonlinear thermoviscous medium. ———Second order, ——— First order.

6.4. Scattering of a plane wave by a finite-circulation vortex

Code validation in case of a non-uniform flow is achieved in the case of a pure tone plane wave propagating through a vortex. This problem has been tackled using both analytical [65, 66, 67] and numerical methods such as parabolic equations [68] or DNS [69]. It has been chosen as a validation case for the Wide-Angle Parabolic Equation of Dallois *et al.* [70] and the FDTD model of Cheinet *et al.* [71, 72]. The vortex has a finite-circulation, its tangential speed is given by:

$$v_\theta(r) = \frac{\Gamma}{2\pi r} \left[1 - exp\left(-\alpha \frac{r^2}{L^2} \right) \right] \tag{61}$$

where r is the distance to the center of the vortex, Γ the circulation and L the size of the vortex. Constant $\alpha = 1.256431$ is chosen so that the maximum velocity occurs at $r = L$. The radial velocity is set to zero. This vortex is an exact solution of the incompressible Navier-Stokes equation, called the

38

Lamb-Oseen vortex. In this work we will present only one configuration: $\Gamma = 1511$, $M = 0.25$ and $L = 2$ m. The wave is generated 40 m before the vortex, its frequency is $f = 43$ Hz. These parameters are chosen to be the same as Colonius *et al.* [69] and Cheinet *et al.* [71]. ~~It is a demanding test case since the Mach number is relatively high while the derivation of the FLHOWARD equation assumes a small Mach number as expected in outdoor acoustics.~~ The computational domain extends from -40 m to 40m in the propagation direction (x), -90 m to 90m in the transverse direction (y) and 0 s to 0.2 s (one period) in time. The boundary conditions used in y are reflections since it was found that they do not interfere with the validation process. The domain is discretized using 2048 points in both x and y directions. 512 points are used for the temporal signal. The mesh is voluntarily oversampled to evaluate only the model. Two computations were performed. The first one tested the FLHOWARD model with operator $FLH^{(2)}$ including the effect of transverse flow $H = H_1 + H2$. Note that in this case $FLH^{(2)} = FLH^{(s)}$. The second omitted the coupling operator H_2 of the algorithm, which is the only one that includes the effect of the transverse flow relative to the main propagation direction. In this case we have $H = H_1$. The results are presented using what Colonius *et al.* called the root-mean-square (RMS) of the scattered field. It consists in subtracting the plane incident field from the results of the computations and then take its RMS value (for a sinusoidal signal it amounts to divide its amplitude by $\sqrt{2}$). Fig. 9 presents the RMS scattered field resulting from FLHOWARD simulation. Two well known features of this case can be observed. First, the effect of refraction due to the finite circulation of the vortex is clearly seen. The scattered field is not zero before entering the vortex. Second, an asymmetry can be observed with an interference pattern due to the fact

that propagation is in the flow direction for $y < 0$ and opposite for $y > 0$. This validates qualitatively the use of FLHOWARD model. Quantitatively, Fig. 9 compares the two FLHOWARD computations (with or without the operator H_2) with Colonius *et al.* DNS results [69]. The value of the field is extracted on a circle of radius 20 m centered on the vortex.

The main maxima and minima are well reproduced even though there are small differences, on the amplitude mostly. The FLHOWARD simulations lead to slightly smoother fluctuations of the pressure field in a way similar to what was observed for scattering by a speed of sound heterogeneity. The main differences between FLHOWARD and DNS are mostly due to the wide-angle approximation on the correction terms that take into account the flow effects. As expected, the transverse flow described by H_2 has only a small effect, only shifting the curves slightly closer to the DNS simulations. The levels of maxima and minima are nearly the same with or without transverse flow.

It is important to emphasize that, for this case, the FLHOWARD model is used at the fringes of its theoretical validity. Indeed, as discussed previously, FLHOWARD model is established for weak flows. In the derivation, the Mach number has been assumed to be less than typically 0.1 because it is designed for acoustic propagation in the atmosphere. Nevertheless, in the section 4.1, it has been shown that the dispersion relation keeps in good agreement with the convected wave equation for relatively high Mach numbers. In the current test case the Mach number is 0.25. This is obviously well beyond the value assumed for the derivation. This large Mach number value is likely to explain the small mismatches between the present approach and reference DNS simulations [69], mostly observed in the location and amplitude of extrema of the scattered field. However, even though

the agreement is not perfect, the results are sufficiently close to DNS ones to provide confidence in our model.

7. Sonic boom at the lateral cutoff

This section illustrates the potential of the developed software through an example of application. The case of sonic boom penetration into the shadow zone at the edge of the primary carpet is chosen. In case of negative vertical temperature gradient or adverse wind, the sonic boom is refracted upwardly and the carpet (footprint of the sonic boom at ground) has a finite width. This is illustrated on Fig. 10. In the shadow zone, the ray theory usually used to evaluate sonic boom [3] cannot predict the signal which results from both diffraction and scattering by turbulence. To model this, an idealized plane wave is propagated through an upwardly refracting atmosphere described by Monin-Obukhov similarity theory giving shear wind and temperature vertical profiles as explained by Ostashev [73]. The case of a mostly sunny day with strong wind [73] is chosen. It corresponds to a surface heat flux $Q_s = 200$ W/m ^{2} and a friction velocity $u_* = 0.7$ m/s. A randomly generated realization 3D turbulent wind field is superposed to the mean atmosphere assuming a homogeneous and isotropic turbulence for simplicity. It obeys a von Kármán energy spectrum and is characterized by two parameters: the characteristic outer scale $L_0 = 100$ m and the level of variance σ_u, three values of which being tested here: $\sigma_u = 1.2, 2.4$ and 3.6 m.s^{-1}. This synthetic turbulent field is generated randomly in the Fourier space according to the method described in [74]. The temporal signal of the incoming wave is extracted from a ray tracing computation of the sonic boom at cut-off of a Mach 5 hypersonic transport vehicle. This aircraft con-
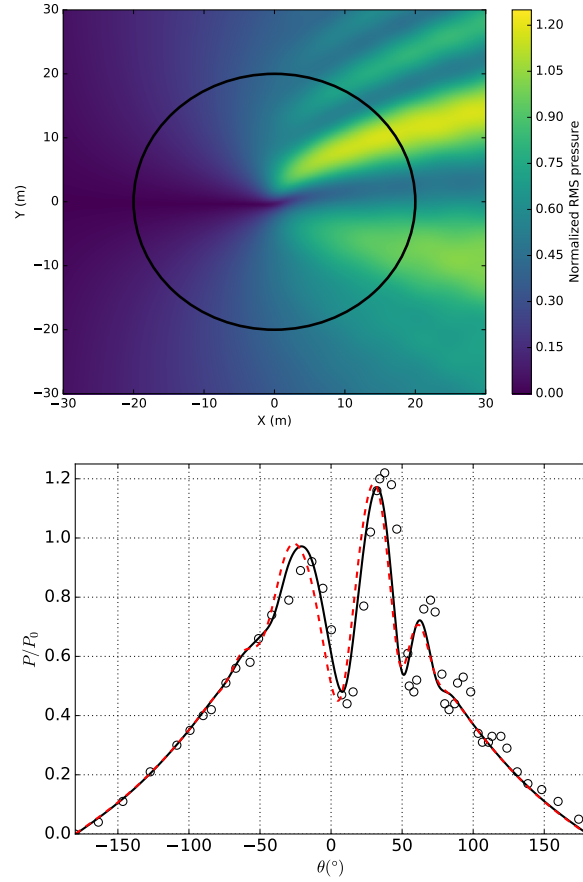
41

Figure 9: Left: normalized RMS pressure amplitude (P_{RMS} - Color level) radiated by the scattering of a plane wave by a finite-circulation vortex. The black circle has a radius of 2.5λ and shows where the pressure is extracted. Right: normalized RMS pressure amplitude radiated by the scattering of a plane wave by a finite-circulation vortex on a circle placed at 2.5λ. $\theta = 0$ is situated on the Ox axis and $\theta = 90$ on the Oy axis. ——— with transverse flow, — — — without transverse flow, circle markers: DNS simulations (Colonius [69]).

.

figuration was described in detail through the European project ATLLAS II [75]. The input signal displays three shocks (one from the nose, one from the wing leading and engine inlets and one from the tail), a duration of about 0.4s and a peak frequency slightly below 2Hz. Propagation is simulated over 4 km along the main horizontal direction Ox, the height and width of the simulation domain being also 4 km. In the vertical direction Oz, an Absorbing Boundary Layer (ABL) of thickness 400 m is imposed on the top of domain. Rigid boundary conditions are imposed on the ground. Laterally, either rigid or periodic boundary conditions can be imposed, with no difference in terms of statistical variability. The duration of the time window is 2.2 s. The temporal signal, the altitude and the transverse direction are sampled with 1024 points each. The maximum frequency of time mesh is therefore 233 Hz. Higher frequency sampling could not be achieved because: (i) the ground rigid boundary condition makes simulation about twice as long as the periodic case; (ii) simulation of multiple realizations is required to achieve statistical convergence. The computational domain has more than 1 billions degrees of freedom; 1024 points are used in the propagation direction.

On Fig. 11 we can observe the progressive decay of the ground positive peak pressure in the central vertical plane ($y = 0$). On the top figure, the atmosphere is stratified but not turbulent and the shadow zone can be clearly seen due to upward refraction against the wind. Just above the shadow zone, a caustic (focusing area) is formed due to the curvature of the initially plane wavefront induced by atmospheric refraction. On the middle figure, for the highest value of turbulence variance $\sigma_u = 3.6$m.s^{-1}, the turbulence is shown to create random variability including multiple focusing and defocusing areas. This process of random scattering also redirects energy into the

43

shadow zone, which turns out to be much less pronounced than in the non turbulent case. As a counterpart, the geometrical caustic tends to smear out. As can be seen on the bottom of Fig.11, the positive peak pressure on the ground surface is still globally decaying with the distance but, due to turbulence, a high variability with areas of enhanced amplitudes is nevertheless observed relatively deep in the shadow zone. Both horizontal and vertical slices show that random caustics are strongly elongated along the main direction of propagation as already known for media without mean flow [35]

Fig. 12 presents two simulated temporal waveforms at $x = 2$ km, either at the ground in the shadow zone ($z = 0$) or near the caustic ($z \approx 250$ m) in cases with or without turbulence. The presence of oscillations before the first shock is due to the periodicity of the time window: the perturbations leaving the time window at the right side are re-injected on the left side. In the shadow zone, without turbulence, the initial N-wave profile progressively smears out along the ground due to exponential attenuation of creeping waves [76, 16]. In the turbulent case, the positive peak pressure is increased and high frequencies associated to the shocks are more strongly scattered from the illuminated to the shadow zones than low frequencies [6]. This results into a very large increase of the wave spectrum with turbulence for frequencies above 5 Hz. Near the caustic the typical U-wave observed without turbulence is strongly affected in the turbulent realization because of the random phase scrambling [77]. As a consequence, the positive peak overpressure is reduced. The spectrum modification changes mostly above 20 Hz, lower frequencies being much less affected.

Finally, to quantify the decrease of positive peak pressure qualitatively seen in Fig. 11, a statistical study is performed. The positive peak pressure
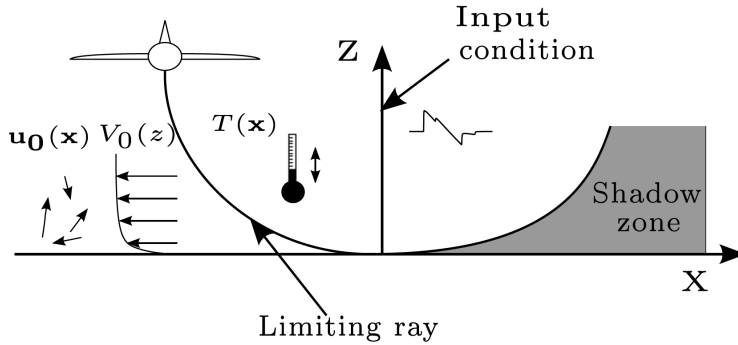
Figure 10: Physical setup for the sonic boom at lateral cutoff

is averaged on the ground along the transverse direction. To get statistical convergence several realizations of turbulence are necessary, here 10 computations for each level of turbulence turned out to be sufficient. Fig. 13 shows the average peak overpressure and its standard deviation compared to the case without turbulence. Both show the classical exponential decay. However, the average positive peak pressure increases with the turbulent intensity as expected because of random scattering from the illuminated zone to the shadow zone. However, even for the highest turbulent intensity, this increase is relatively small (no more than 5 Pa) because turbulence affects only the upper part of the signal spectrum. The standard deviation first increases over distances in the range from 500 m to 1000 m before slowly decaying. This behaviour is similar to what happens for free field turbulence, but the amplitude of the deviation is much weaker. Again, the more intense the turbulence, the more standard deviation increases.
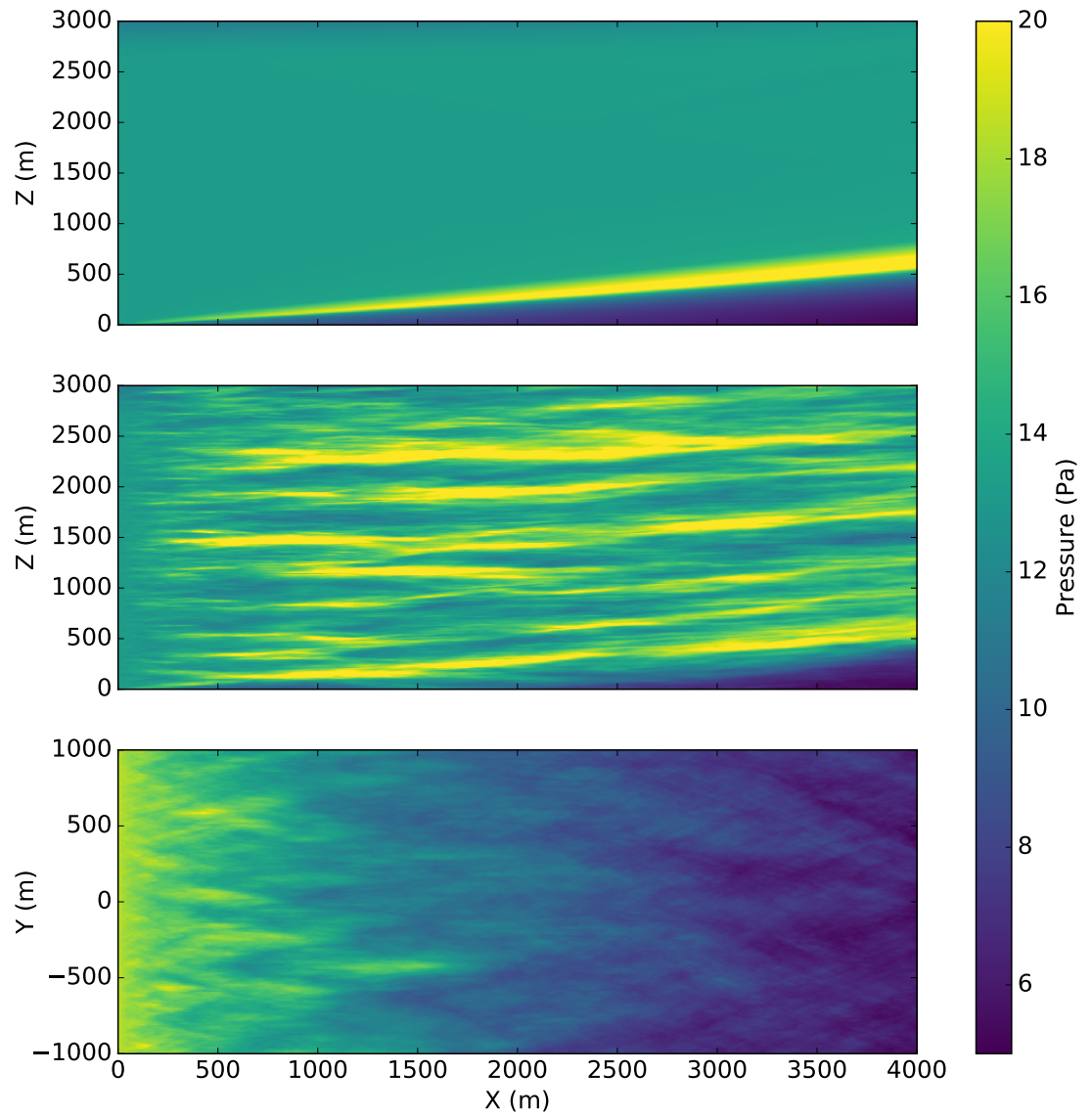
Figure 11: Maximum pressure field in a vertical plane without (top) and with atmospheric turbulence ($\sigma_u = 3.6\text{m.s}^{-1}$) (middle) and on the ground with atmospheric turbulence ($\sigma_u = 3.6\text{m.s}^{-1}$) (bottom).
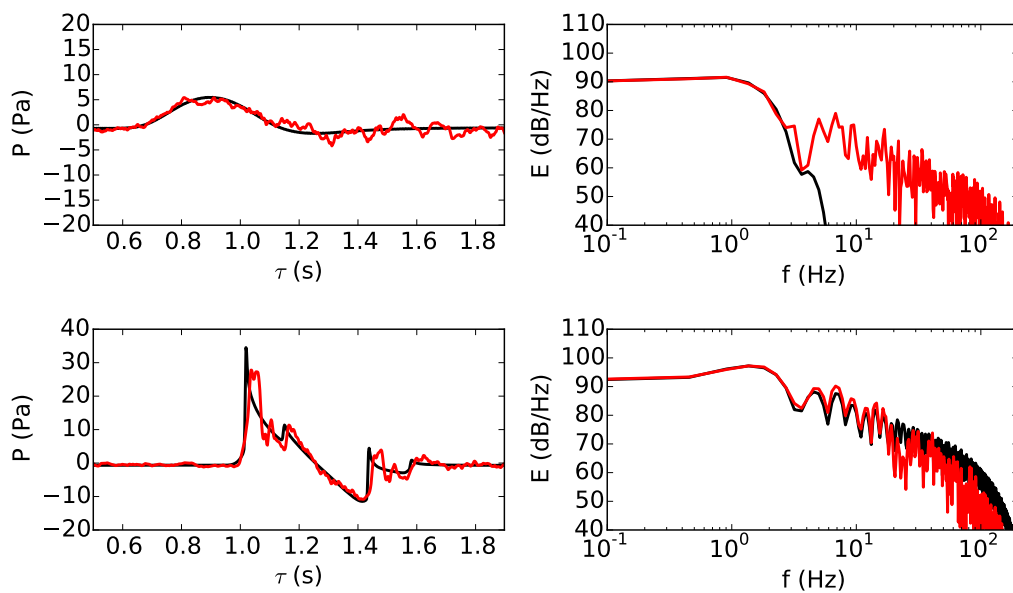
Figure 12: Examples of pressure signals (left) and their spectra (right): in the shadow zone (top) and near caustic (bottom). Black/red lines: without/with turbulence ($\sigma_u = 3.6\text{m.s}^{-1}$).
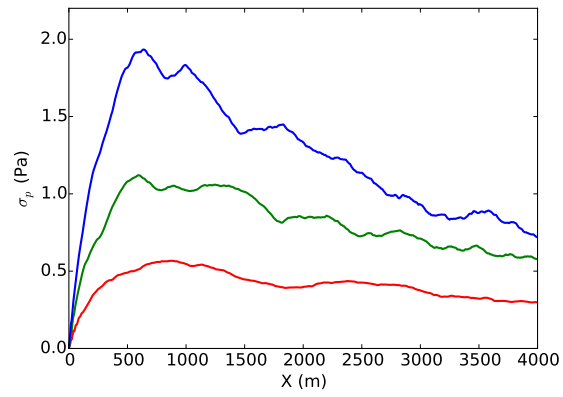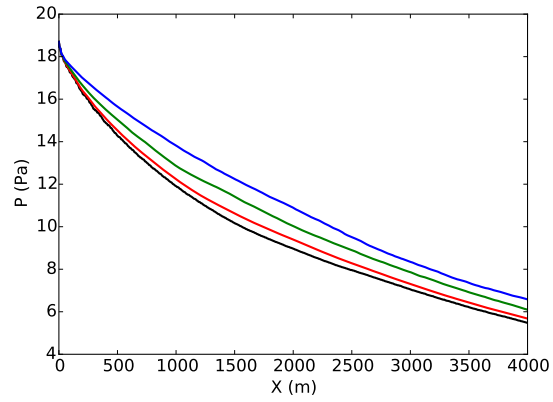
Figure 13: Average (left) and standard deviation (right) of the peak pressure along the propagation axis Ox for different turbulent intensities. Black: $\sigma_u = 0\text{m.s}^{-1}$, red: $\sigma_u = 1.2\text{m.s}^{-1}$, green: $\sigma_u = 2.4\text{m.s}^{-1}$; blue: $\sigma_u = 3.6\text{m.s}^{-1}$

8. Conclusion

An original three-dimensional one-way method has been developed to model and simulate the nonlinear propagation of acoustic shock waves in the atmosphere. It relies on a scalar wave equation which includes diffraction, flow and heterogeneities effects, nonlinearity, thermoviscous absorption, molecular relaxation and rigid reflexion over a flat ground. The model strives to be as high order as possible while remaining computationally tractable. To achieve this, numerical approach relies on the fractional step method which permits to solve different simpler problems using algorithms that are as efficient as possible. When possible, spectral or analytical solutions are employed. For the other terms, finite differences method is used. To asses the validity and accuracy of the resulting FLHOWARD3D software, its dispersion relation, including the split-step scheme, was established and shown to be exact up to order $M^2\bar{k}_z^4$, so of second order relative to the flow Mach number M and fourth order relative to the propagation angle measured by the dimensionless wavenumber $\bar{k}_z$. Rigid ground and free field boundary conditions have been implemented. The algorithm is implemented for high performance computing on distributed memory architecture. The model and its implementation have been validated by quantitative test cases involving all the operators and boundary conditions. Results turn out excellent, even in cases were the model was used outside its theoretical range of validity. The biggest approximation of the method in terms of results accuracy is the neglecting of the field backscattering in the inhomogeneous case. Nevertheless this one-way approximation allows to handle problems with a very high number of Degrees of Freedom. Large scale problems are tackled with parallelization performances showing again an excellent behav-

ior for both weak and strong scaling. Finally, an example of application was performed. The computation of the sonic boom at the shadow zone and influence of turbulence was chosen. All the phenomena relatives to scattering of a wave in a shadow zone were retrieved. It demonstrates that FLHOWARD 3D is well suited for the simulation of acoustical shock waves on relatively long distance of propagation through media with scalar and vectorial heterogeneities.

9. Acknowledgments

Appendix A. Expression of operator H

Expression for operator $FLH^{(1)}$ is:

$$
\begin{aligned}
FLH^{(1)}\phi(\mathbf{x}, \tau) = {} & \frac{V_{0x}}{\bar{c}_0{}^2} \frac{\partial \phi}{\partial \tau} - \frac{V_{0x}}{\bar{c}_0} \frac{\partial \phi}{\partial x} - \frac{V_{0y}}{\bar{c}_0} \frac{\partial \phi}{\partial y} \\
& + \frac{V_{0x}^2}{2\bar{c}_0} \int_{-\infty}^{\tau} \left(\frac{\partial^2 \phi}{\partial y^2} + \frac{\partial^2 \phi}{\partial z^2} \right) d\tau' - \frac{V_{0x}^2}{2\bar{c}_0{}^3} \frac{\partial \phi}{\partial \tau} \\
& + \frac{V_{0x}V_{0y}}{\bar{c}_0} \left(\frac{1}{\bar{c}_0} \frac{\partial \phi}{\partial y} - \int_{-\infty}^{\tau} \frac{\partial^2 \phi}{\partial x \partial y} d\tau' \right) - \frac{V_{0y}^2}{2\bar{c}_0} \int_{-\infty}^{\tau} \frac{\partial^2 \phi}{\partial y^2} d\tau' \\
& + \bar{c}_0 V_{0x} \int_{-\infty}^{\tau} \int_{-\infty}^{\tau} \frac{\partial^3 \phi}{\partial x \partial z^2} d\tau' d\tau' - \bar{c}_0 \int_{-\infty}^{\tau} \int_{-\infty}^{\tau} \frac{\partial}{\partial z} \left[V_{0x} \frac{\partial^2 \phi}{\partial x \partial z} \right] d\tau' d\tau' \\
& + \int_{-\infty}^{\tau} \frac{d}{dz} \left[V_{0x} \frac{\partial \phi}{\partial z} \right] d\tau' - V_{0x} \int_{-\infty}^{\tau} \frac{\partial^2 \phi}{\partial z^2} d\tau' \\
& + \bar{c}_0 V_{0y} \int_{-\infty}^{\tau} \int_{-\infty}^{\tau} \frac{\partial^3 \phi}{\partial y \partial z^2} d\tau' d\tau' - \bar{c}_0 \int_{-\infty}^{\tau} \int_{-\infty}^{\tau} \frac{\partial}{\partial z} \left[V_{0y} \frac{\partial^2 \phi}{\partial y \partial z} \right] d\tau' d\tau'.
\end{aligned}
\tag{A.1}
$$

First line of Eq. A.1 describes linear convection terms by the mean stratified flow. The second and third lines are for the nonlinear quadratic convection terms. The last three lines emanate from the gradient of the ambient flow.

Expression for operator $FLH^{(2)}$ is:

$$
FLH^{(2)}\phi(\mathbf{x}, \tau) = \frac{u_{0x}}{\bar{c}_0{}^2} \frac{\partial \phi}{\partial \tau} - \frac{u_{0x}}{\bar{c}_0} \frac{\partial \phi}{\partial x} - \frac{u_{0y}}{\bar{c}_0} \frac{\partial \phi}{\partial y} - \frac{u_{0z}}{\bar{c}_0} \frac{\partial \phi}{\partial z}.
\tag{A.2}
$$

Eq. A.2 takes only into account the linear convection effects due to the flow fluctuations.

Expression for operator TH is:

$$TH\phi(\mathbf{x}, \tau) = \frac{1}{2\rho_0} \left(\frac{\partial \rho_0}{\partial x} \phi - \bar{c}_0 \int_{-\infty}^{\tau} \frac{\partial \rho_0}{\partial x} \frac{\partial \phi}{\partial x} d\tau' \right)$$
$$- \frac{\bar{c}_0}{2\rho_0} \int_{-\infty}^{\tau} \left(\frac{\partial}{\partial y} \left[\rho_0 \frac{\partial \phi}{\partial y} \right] + \frac{\partial}{\partial z} \left[\rho_0 \frac{\partial \phi}{\partial z} \right] \right) d\tau' + \frac{\bar{c}_0}{2} \int_{-\infty}^{\tau} \left(\frac{\partial^2 \phi}{\partial y^2} + \frac{\partial^2 \phi}{\partial z^2} \right) d\tau'$$
$$+ \frac{2\bar{c}_0 c_0' + c_0'^2}{2\bar{c}_0{}^3} \frac{\partial \phi}{\partial \tau}, \qquad\qquad (A.3)$$

The first line of Eq. A.3 stands for the density heterogeneities in the main propagation direction x, the second line for those in the transverse directions y and z. The last term takes into account all effects due to sound speed heterogeneities. Note that in the definitions of $FLH^{(1)}$ (Eq. A.1), $FLH^{(2)}$ (Eq. A.2) and TH (Eq. A.3) the components V_{0x}, u_{0x} and $\partial \rho_0 / \partial x$ appear differently from the other ones because of the introduction of retarded time in the main propagation direction x.

Appendix B. Numerical implementation of H_2.

As explained in 3.4, operator H_2 is solved using a second order finite difference method in the frequency domain. In the x-direction, a semi-implicit Crank-Nicolson scheme is used. It is unconditionally stable and of second order accuracy. The resulting linear system is split into the y and z directions using an Alternate Direction Implicit (ADI) method. For the z-direction the equation to solve takes the form of the following linear system:

$$\mathbf{A} \cdot \mathbf{u} = \mathbf{q} \qquad\qquad (B.1)$$

where $\mathbf{A}$ is the tridiagonal matrix:

$$\mathbf{A} = \begin{pmatrix} a_{j,0} & c_{j,0} & 0 & \cdots & \cdots & \cdots & 0 \\ b_{j,1} & \ddots & \ddots & \ddots & & & \vdots \\ 0 & \ddots & \ddots & \ddots & \ddots & & \vdots \\ \vdots & \ddots & b_{j,k} & a_{j,k} & c_{j,k} & \ddots & \vdots \\ \vdots & & \ddots & \ddots & \ddots & \ddots & 0 \\ \vdots & & & \ddots & b_{j,nz-2} & a_{j,nz-2} & c_{j,nz-2} \\ 0 & \cdots & \cdots & \cdots & 0 & b_{j,nz-1} & a_{j,nz-1} \end{pmatrix}. \qquad (\text{B.2})$$

Its coefficients are given by:

$$a_{j,k} = 1 + \frac{\bar{c}_0}{\omega^2 \Delta z^2} \left[-2V_{0x} + V^i_{0x\,k+1/2} + V^i_{0x\,k-1/2} \right]$$
$$+ \frac{i\theta\Delta x}{\omega\Delta z^2} \left[-\frac{V^2_{0x}}{\bar{c}_0} + 2V_{0x} + \frac{\bar{c}_0\rho_{0j,k+1/2}}{2\rho_0} + \frac{\bar{c}_0\rho_{0j,k-1/2}}{2\rho_0} - \bar{c}_0 - V_{0xk+1/2} - V_{0xk-1/2} \right]$$
$$(\text{B.3})$$

$$b_{j,k} = \frac{\bar{c}_0}{\omega^2 \Delta z^2} \left[V_{0x} - V_{0x\,k-1/2} \right]$$
$$+ \frac{i\theta\Delta x}{\omega\Delta z^2} \left[\frac{V^2_{0x}}{2\bar{c}_0} - V_{0x} - \frac{\bar{c}_0\rho_{0j,k-1/2}}{2\rho_0} + \frac{\bar{c}_0}{2} + V_{0xk-1/2} \right], \qquad (\text{B.4})$$

$$c_{j,k} = \frac{\bar{c}_0}{\omega^2 \Delta z^2} \left[V_{0x} - V_{0x\,k+1/2} \right]$$
$$+ \frac{i\theta\Delta x}{\omega\Delta z^2} \left[\frac{V^2_{0x}}{2\bar{c}_0} - V_{0x} - \frac{\bar{c}_0\rho_{0j,k+1/2}}{2\rho_0} + \frac{\bar{c}_0}{2} + V_{0xk+1/2} \right]. \qquad (\text{B.5})$$

q coefficients are:

$$q_{j,k} = \widehat{\phi}_{j,k-1}^{i-1}\frac{\bar{c}_0}{\omega^2\Delta z^2}\left[V_{0x} - V_{0x\,j,k-1/2}\right] - \widehat{\phi}_{j,k-1}^{i-1}\frac{(1-\theta)i\Delta x}{\omega\Delta z^2}\left[\frac{V_{0x}^2}{2\bar{c}_0} - V_{0x} - \frac{\bar{c}_0\rho_{0j,k-1/2}}{2\rho_0} + \frac{\bar{c}_0}{2} + V_{0xk-1/2}\right]$$

$$+ \widehat{\phi}_{j,k}^{i-1}\left[1 + \frac{\bar{c}_0}{\omega^2\Delta z^2}\left(-2V_{0x} + V_{0x\,j,k-1/2} + V_{0x\,j,k+1/2}\right)\right]$$

$$- \widehat{\phi}_{j,k}^{i-1}\frac{(1-\theta)i\Delta x}{\omega\Delta z^2}\left[-\frac{V_{0x}^2}{\bar{c}_0} + 2V_{0x} - V_{0xk+1/2} - V_{0xk-1/2}\right] - \widehat{\phi}_{j,k}^{i-1}\frac{(1-\theta)i\Delta x}{\omega\Delta z^2}\left[+\frac{\bar{c}_0\rho_{0j,k+1/2}}{2\rho_0} + \frac{\bar{c}_0\rho_{0j,k}}{2\rho_0}\right.$$

$$+ \widehat{\phi}_{j,k+1}^{i-1}\frac{\bar{c}_0}{\omega^2\Delta z^2}\left[V_{0x} - V_{0x\,j,k+1/2}\right] - \widehat{\phi}_{j,k+1}^{i-1}\frac{(1-\theta)i\Delta x}{\omega\Delta z^2}\left[+\frac{V_{0x}^2}{2\bar{c}_0} - V_{0x} - \frac{\bar{c}_0\rho_{0j,k+1/2}}{2\rho_0} + \frac{\bar{c}_0}{2} + V_{0xk+1/2}\right]$$

$$\text{(B.6)}$$

This system is solved using Thomas algorithm for tridiagonal linear systems.

The method is similar for the y-direction.

Appendix C. Analytical solution for the validations

Appendix C.1. Acoustic piston

Axial field $\widehat{p}_a(x, y = z = 0)$ at angular frequency ω is given in terms of wavenumber $k = \omega/c_0$ by:

$$\widehat{p}_a(x, y = z = 0) = \widehat{p}_0\left(\exp(ikx) - \frac{x\exp(ik\sqrt{x^2+a^2})}{\sqrt{x^2+a^2}}\right) \qquad \text{(C.1)}$$

with $\widehat{p}_0$ the pressure amplitude on the piston surface and a the piston radius.

Appendix C.2. Scattering by a sphere

Let us consider the scattering of an incident plane wave of angular frequency ω in a fluid of density ρ_0 and sound speed c_0 by a fluid sphere of radius a, density ρ_h and sound speed c_h located at the origin. The incident plane wave can be expanded into a series of spherical harmonics:

$$p_{inc} = P_0 \sum_{m=0}^{\infty} i^m(2m+1)P_m(\cos\theta)j_m(k_0r)\exp(-i\omega t), \qquad \text{(C.2)}$$

54

when written in spherical coordinates (r, θ, ϕ) with $\theta = 0$ being the wave axis of propagation so that the problem is independant of ϕ. The scattered field in the outer fluid with $p = p_{inc} + p_{sc}$ for $r > a$ is given by

$$p_{sc} = \sum_{m=0}^{\infty} A_m P_m(\cos\theta) h_m(k_0 r) \exp(-i\omega t), \tag{C.3}$$

while the transmitted field within the spherical heterogeneity $(r < a)$

$$p_t = \sum_{m=0}^{\infty} B_m P_m(\cos\theta) j_m(k_h r) \exp(-i\omega t). \tag{C.4}$$

Here P_m are the Legendre polynomials, j_m the spherical Bessel functions, $h_m(x) = j_m(x) + i n_m(x)$ the spherical Hankel functions and n_m the spherical Neumann functions. Wave number is $k_0 = \omega/c_0$ in the outer fluid and $k_h = \omega/c_h$ in the sphere. Coefficients A_m and B_m are given by:

$$A_m = P_0 i^m (2m+1) \frac{st[j_m(k_h a)\alpha_m(ka)] - j_m(ka)\alpha_m(k_h a)}{\alpha_m(k_h a) h_m(ka) - st[\alpha_m(ka) + i\beta_m(ka)] j_m(k_h a)}, \tag{C.5}$$

$$B_m = \frac{st A_m}{\alpha_m(k_h a)} (\alpha_m(ka) + i\beta_m(ka)) + st P_0 i^m (2m+1) \frac{\alpha_m(ka)}{\alpha_m(k_h a)}, \tag{C.6}$$

with $s = c_h/c_0$ and $t = \rho_h/\rho_0$, while $\alpha_m(x) = m j_{m-1}(x) - (m+1) j_{m+1}(x)$ and $\beta_m(x) = m n_{m-1}(x) - (m+1) n_{m+1}(x)$.

Appendix C.3. Nonlinear propagation in a thermoviscous medium

The solution of Burgers' equation:

$$\frac{\partial P}{\partial \sigma} = P \frac{\partial P}{\partial \tau} + \frac{1}{\Gamma} \frac{\partial^2 P}{\partial \tau^2} \tag{C.7}$$

with input condition $P(\sigma = 0, \tau) = \sin(\tau)$ is given by:

$$P(\sigma, \tau) = \frac{2}{\Gamma} \frac{\sum_{n=1}^{\infty} \epsilon_n (-1)^{n+1} n I_n(\Gamma/2) \exp(-n^2 \sigma/\Gamma) \sin(n\tau)}{\sum_{n=0}^{\infty} \epsilon_n (-1)^n I_n(\Gamma/2) \exp(-n^2 \sigma/\Gamma) \cos(n\tau)}. \tag{C.8}$$

with ϵ_n Neumann factor equal to 2 for $n \geq 1$ and 1 for $n = 0$, and with $I_n(x) = i^{-n} J_n(ix)$ the modified Bessel function of the first kind.

[1] V. E. Ostashev, Acoustics in Moving Inhomogeneous Media, E&FN Spon, London, 1997.

[2] L. Evers, H. W. Haak, The characteristics of infrasound, its propagation and some early history, in: A. Le Pichon, E. Blanc, A. Hauchecorne (Eds.), Infrasound Monitoring for Atmospheric Studies, Springer, Dordrecht, 2010, pp. 3–27.

[3] K. J. Plotkin, State of the art of sonic boom modeling, The Journal of the Acoustical Society of America 111 (1) (2002) 530–536.

[4] R. Blumrich, F. Coulouvrat, D. Heimann, Meteorologically induced variability of sonic-boom characteristics of supersonic aircraft in cruising flight, The Journal of the Acoustical Society of America 118 (2) (2005) 707–722.

[5] A. Loubeau, F. Coulouvrat, Effects of Meteorological Variability on Sonic Boom Propagation from Hypersonic Aircraft, AIAA Journal 47 (11) (2009) 2632–2641.

[6] S. C. Crow, Distortion of sonic bangs by atmospheric turbulence, Journal of Fluid Mechanics 37 (3) (1969) 529–563.

[7] A. D. Pierce, D. J. Maglieri, Effects of Atmospheric Irregularities on Sonic-Boom Propagation, The Journal of the Acoustical Society of America 51 (2) (1972) 702–721.

[8] A. McAlpine, M. J. Fisher, on the Prediction of "Buzz-Saw" Noise in Aero-Engine Inlet Ducts, Journal of sound and vibration 248 (1) (2001) 123–149.

[9] R. Fernando, Y. Druon, F. Coulouvrat, R. Marchiano, Nonlinear waves and shocks in a rigid acoustical guide., The Journal of the Acoustical Society of America 129 (2) (2011) 604–15.

[10] K. L. Gee, V. W. Sparrow, M. M. James, J. M. Downing, C. M. Hobbs, T. B. Gabrielson, A. A. Atchley, The role of nonlinear effects in the propagation of noise from high-power jet aircraft., The Journal of the Acoustical Society of America 123 (6) (2008) 4082–4093.

[11] H. E. Bass, The propagation of thunder through the atmosphere, The Journal of the Acoustical Society of America 67 (6) (1980) 1959–1966.

[12] M. Henneton, O. Gainville, F. Coulouvrat, Numerical Simulation of Sonic Boom from Hypersonic Meteoroids, AIAA Journal 53 (9) (2015) 2560–2570.

[13] O. Gainville, Modélisation de la propagation atmosphérique des ondes infrasonores par une méthode de tracé de rayons non linéaire (in french), Ph.D. thesis, Ecole Centrale de Lyon (2008).

[14] W. Hayes, R. Haefeli, H. Kulsrud, Sonic boom propagation in a stratified atmosphere with computer program, Tech. rep., NASA CR-1299 (1969).

[15] A. D. Pierce, Acoustics: an introduction to its physical principles and applications, Acoustical Society of America, 1981.

[16] F. Coulouvrat, Sonic boom in the shadow zone: A geometrical theory of diffraction, The Journal of the Acoustical Society of America 111 (1) (2002) 499–508.

[17] R. Marchiano, F. Coulouvrat, R. Grenon, Numerical simulation of shock wave focusing at fold caustics, with application to sonic boom, The Journal of the Acoustical Society of America 114 (4) (2003) 1758–1771.

[18] R. Marchiano, J.-L. Thomas, F. Coulouvrat, Experimental simulation of supersonic superboom in a water tank: nonlinear focusing of weak shock waves at a fold caustic., Physical review letters 91 (18) (2003) 184301.

[19] R. Marchiano, F. Coulouvrat, J.-L. Thomas, Nonlinear focusing of acoustic shock waves at a caustic cusp., The Journal of the Acoustical Society of America 117 (2) (2005) 566–577.

[20] C. Tam, J. Webb, Dispersion-Relation-Preserving Finite Difference Schemes for Computational Acoustics, Journal of Computational Physics 107 (2) (1993) 262–281.

[21] C. Bogey, C. Bailly, A family of low dispersive and low dissipative explicit schemes for flow and noise computations, Journal of Computational Physics 194 (1) (2004) 194–214.

[22] V. W. Sparrow, R. Raspet, A numerical method for general finite amplitude wave propagation in two dimensions and its application to spark pulses, The Journal of the Acoustical Society of America 90 (5) (1991) 2683–2691.

[23] S. Del Pino, B. Després, P. Havé, H. Jourdren, P. Piserchia, 3D Finite Volume simulation of acoustic waves in the earth atmosphere, Computers & Fluids 38 (4) (2009) 765–777.

[24] O. Marsden, C. Bogey, C. Bailly, A study of infrasound propagation based on high-order finite difference solutions of the Navier-Stokes equations., The Journal of the Acoustical Society of America 135 (3) (2014) 1083–95.

[25] R. Yamashita, K. Suzuki, Full-Field Simulation for Sonic Boom Cuto ff Phenomena, Trans. Japan Soc. Aero. Space Sci. 58 (6) (2015) 327–336.

[26] A. Towne, T. Colonius, One-way spatial integration of hyperbolic equations, Journal of Computational Physics 300 (2015) 844–861.

[27] F. D. Tappert, The parabolic approximation method, in: Wave propagation and underwater acoustics, Springer, 1977, pp. 224–287.

[28] J. F. Claerbout, Coarse grid calculations of waves in inhomogeneous media with application to delineation of complicated seismic structure, Geophysics 35 (3) (1970) 407–418.

[29] E. V. Zabolotskaya, R. V. Khokhlov, Quasi-plane waves in the nonlinear acoustics of confined beams, Sov. Phys. Acoust. 15 (1969) 35–40.

[30] V. P. Kuznetsov, Equations of nonlinear acoustics, Sov. Phys. Acoust. 15 (1970) 467–470.

[31] Y.-S. Lee, M. F. Hamilton, Time-domain modeling of pulsed finite-amplitude sound beams, The Journal of the Acoustical Society of America 97 (2) (1995) 906–917.

[32] Y. Jing, R. O. Cleveland, Modeling the propagation of nonlinear three-dimensional acoustic beams in inhomogeneous media., The Journal of the Acoustical Society of America 122 (3) (2007) 1352–1364.

[33] B. K. Novikov, O. V. Rudenko, V. I. Timoshenko, Nonlinear Underwater Acoustics, Acoustical Society of America, New York, 1987.

[34] M. V. Averiyanov, V. A. Khokhlova, O. A. Sapozhnikov, P. Blanc-Benon, R. O. Cleveland, Parabolic equation for nonlinear acoustic wave propagation in inhomogeneous moving media, Acoustical Physics 52 (6) (2006) 623–632.

[35] M. Averiyanov, P. Blanc-Benon, R. O. Cleveland, V. A. Khokhlova, Nonlinear and diffraction effects in propagation of N-waves in randomly inhomogeneous moving media., The Journal of the Acoustical Society of America 129 (4) (2011) 1760–1772.

[36] P. T. Christopher, K. J. Parker, New approaches to the linear propagation of acoustic fields., The Journal of the Acoustical Society of America 90 (1) (1991) 507–521.

[37] T. Varslot, G. Taraldsen, Computer simulation of forward wave propagation in soft tissue., IEEE Transactions on Ultrasonics, Ferroelectrics and Frequency Control 52 (9) (2005) 1473–1482.

[38] F. Dagrau, M. Rénier, R. Marchiano, F. Coulouvrat, Acoustic shock wave propagation in a heterogeneous medium: a numerical simulation beyond the parabolic approximation., The Journal of the Acoustical Society of America 130 (1) (2011) 20–32.

[39] R. J. Zemp, J. Tavakkoli, R. S. C. Cobbold, Modeling of nonlinear ultrasound propagation in tissue from array transducers., The Journal of the Acoustical Society of America 113 (1) (2003) 139–152.

[40] L.-J. Gallin, M. Rénier, E. Gaudard, T. Farges, R. Marchiano, F. Coulouvrat, One-way approximation for the simulation of weak shock wave propagation in atmospheric flows., The Journal of the Acoustical Society of America 135 (5) (2014) 2559–70.

[41] R. B. Stull, An introduction to boundary layer meteorology, Springer, Amsterdam, 1988.

[42] D. K. Wilson, D. W. Thomson, Acoustic propagation through anisotropic, surface-layer turbulence, The Journal of the Acoustical Society of America 96 (August 1994) (1994) 1080–1095.

[43] F. Coulouvrat, New equations for nonlinear acoustics in a low Mach number and weakly heterogeneous atmosphere, Wave Motion 49 (1) (2012) 50–63.

[44] F. Coulouvrat, A quasi-analytical shock solution for general nonlinear progressive waves, Wave Motion 46 (2) (2009) 97–107.

[45] N. N. Yanenko, The method of fractional steps, Springer-Verlag, Berlin, 1971.

[46] H. Holden, K. H. Karlsen, K.-A. Lie, N. H. Risebro, Splitting methods for partial differential equations with rough solutions, European Mathematical Society, Zurich, 2010.

[47] G. Strang, On the construction and comparison of difference schemes, SIAM Journal on Numerical Analysis 5 (3) (1968) 506–517.

[48] J. W. Goodman, Introduction to Fourier Optics, McGraw and Hill, New York, 1968.

[49] FFTW official website, `http://www.fftw.org/`, accessed 17 january 2017.

[50] L.-J. Gallin, Caractérisation acoustique des éclairs d'orage, Ph.D. thesis, Université Pierre et Marie Curie Paris VI (2014).

[51] A. Quarteroni, R. Sacco, F. Saleri, Numerical mathematics, Springer-Verlag, New York, 2007.

[52] J. Burgers, Further statistical problems connected with the solution of a simple nonlinear partial differential equation, Proc. Kon. Nederlandse Akad. van Wet. Ser. (B 57) (1954) 159–169.

[53] M. F. Hamilton, D. T. Blackstock, Nonlinear acoustics, Academic Press, 1998.

[54] L. C. Sutherland, H. E. Bass, Atmospheric absorption in the atmosphere up to 160 km, The Journal of the Acoustical Society of America 115 (3) (2004) 1012–1032.

[55] R. O. Cleveland, M. F. Hamilton, D. T. Blackstock, Time-domain modeling of finite-amplitude sound in relaxing fluids, The Journal of the Acoustical Society of America 99 (June) (1996) 3312–3318.

[56] ISO, Acoustics - Attenuation of sound during propagation outdoors - Part 1: Calculation of the absorption of sound by the atmosphere, Tech. rep., International Organization for Standardization, Geneva, Switzerland (1993).

[57] P. M. Morse, K. U. Ingard, Theoretical acoustics, McGraw-Hill, New York, 1968.

[58] B. Fornberg, A practical guide to pseudospectral methods, Cambridge University Press, 1996.

[59] G. D. Dockery, J. R. Kuttler, An improved impedance-boundary algorithm for Fourier split-step solutions of the parabolic wave equation, IEEE Transactions on Antennas and Propagation 44 (12) (1996) 1592–1599.

[60] F. Collino, Perfectly matched absorbing layers for the paraxial equations, Journal of Computational Physics 180 (1997) 164–180.

[61] G. Cohen, Higher-Order Numerical Methods for Transient Wave Equations, Springer, Berlin, 2002.

[62] M. Averiyanov, Propagation des ondes acoustiques à travers un milieu turbulent: Etudes théorique et expériementale des effets de diffraction et des effets non linéaire, Ph.D. thesis, Ecole Centrale de Lyon (2008).

[63] D. Pekurovsky, P3dfft: A framework for parallel computations of fourier transforms in three dimensions, SIAM Journal on Scientific Computing 34 (4) (2012) C192–C209.

[64] V. C. Anderson, Sound scattering from a fluid sphere, The Journal of the Acoustical Society of America 22 (July) (1950) 426–431.

[65] S. O'shea, Sound scattering by a potential vortex, Journal of Sound and Vibration 43 (1) (1975) 109–116.

[66] R. Ford, S. G. Llewellyn Smith, Scattering of acoustic waves by a vortex, Journal of Fluid Mechanics 386 (1999) 305–328.

[67] M. Howe, On the scattering of sound by a rectilinear vortex, Journal of sound and vibration 227 (1999) 1003–1017.

[68] S. M. Candel, Numerical solution of wave scattering problems in the parabolic approximation, Journal of Fluid Mechanics 90 (3) (1979) 465–507.

[69] T. Colonius, S. K. Lele, P. Moin, The scattering of sound waves by a vortex: numerical simulations and analytical solutions, Journal of Fluid Mechanics 260 (1994) 271–298.

[70] L. Dallois, P. Blanc-Benon, Wide angle parabolic equations in moving media: Sound diffraction by a core vortex, AIAA Paper 2001-2256 (2001) 856–864.

[71] S. Cheinet, L. Ehrhardt, D. Juvé, P. Blanc-Benon, Unified modeling of turbulence effects on sound propagation., The Journal of the Acoustical Society of America 132 (4) (2012) 2198–209.

[72] L. Ehrhardt, Modélisation en domaine temporel de la propagation acoustique, Ph.D. thesis, Ecole Centrale de Lyon (2013).

[73] V. E. Ostashev, M. V. Scanlon, D. K. Wilson, S. N. Vecherin, Source localization from an elevated acoustic sensor array in a refractive atmosphere., The Journal of the Acoustical Society of America 124 (6) (2008) 3413–3420.

[74] R. Frehlich, L. Cornman, R. Sharman, Simulation of Three-Dimensional

Turbulent Velocity Fields, Journal of Applied Meteorology 40 (2) (2001) 246–258.

[75] D. Luquet, R. Marchiano, F. Coulouvrat, I. Salah El Din, A. Loseille, Sonic Boom Assessment of a Hypersonic Transport Vehicle with Advanced Numerical Methods, AIAA Paper 2015-2685 (2015) 1–13.

[76] A. Berry, G. A. Daigle, Controlled experiments of the diffraction of sound by a curved, The Journal of the Acoustical Society of America 83 (6) (1988) 2047–2058.

[77] A. D. Pierce, Statistical Theory of Atmospheric Turbulence Effects on Sonic-Boom Rise Times, The Journal of the Acoustical Society of America 49 (3) (1971) 906–924.